Chapter 12

Dynamic Characterization of Adhesive Materials for Vibration Control

Jon García-Barruetabeña and
Fernando Cortés Martínez

Additional information is available at the end of the chapter

http://dx.doi.org/10.5772/66104

Abstract

This chapter focuses on the dynamic characterization of adhesive materials for vibration control proposes. First, the experimental characterization and modelization of the relaxation and complex moduli of the flexible adhesive ISR 70-03 by means of a dynamic mechanical thermal analysis technique (DMTA) are presented. Then, the interconversion path between the relaxation modulus $E(t)$ and the corresponding complex modulus $E^*(\omega)$ for linear viscoelastic solid materials is explored. In contrast to other approximate methods, in this work the fast Fourier transform (FFT) algorithm is directly applied on relaxation functions. Finally, an experimental study for the structural noise and vibration reduction in a cabin elevator by means of adhesive-bonded joints of panels is presented.

Keywords: elastomers and rubber, nondestructive testing, relaxation modulus, complex modulus, viscoelasticity, material functions interconversion, noise and vibration reduction, adhesive-bonded joints

1. Introduction

Regarding damping, joint procedures by means of screws, rivets, or by joining do not introduce relevant damping outside of some specific frequency ranges [1–5]. Therefore, they are not relevant for vibration control porpoises. However, adhesive joint can be designed for structural noise control because they are able tointroduce effective modal damping below 1 kHz [6].

In particular, viscoelastic adhesives are widely employed in engineering applications and also found their widespread application in many sectors such as the automotive industry, aerospace, wind power, and human transportation. The mechanical properties of general viscoelastic materials depend on temperature, frequency and amplitude, prestress, dynamic load

level, relative humidity, and among others. Service temperature, frequency, and amplitude of deformation are the most relevant ones. Thus, suitable mechanical characterization is essential in order to obtain reliable predictions.

2. Experimental characterization of a flexible adhesive

The experimental characterization by means of adynamic mechanical thermal analysis technique (DMTA) and the modelization of the relaxation and complex moduli of the flexible adhesive ISR 70-03 [7] are presented. The manufacturing procedure of the test experiments is detailed. Then, the influence of the strain level and specimen thickness into material behavior is studied. Next, using a procedure based on the time-temperature superposition principle, relaxation and dynamic master curves under tension strain are obtained. Finally, a generalized Maxwell model and a fractional derivative model of these master curves are implemented. As a conclusion, models capable of describing together the influence of time, temperature, and strain level are proposed.

Flexible adhesive shows viscoelastic behavior [8, 9]. In these viscoelastic materials (VEMs), the energy dissipation is a consequence of the phase difference between the stress σ and the strain ε. In frequency domain, this behavior is represented by the complex modulus approximation, which can be obtained from the relationship between the harmonic stress $\sigma(t)$

$$\sigma(t) = \sigma_0 \mathrm{e}^{\mathrm{i}\omega t} \tag{1}$$

and the stationary harmonic strain $\varepsilon(t)$ given by

$$\varepsilon(t) = \varepsilon_0 \mathrm{e}^{\mathrm{i}(\omega t - \varphi)} \tag{2}$$

σ_0 is the stress amplitude, ε_0 is the strain amplitude, ω is the excitation frequency, and φ is the phase delay. Therefore, the frequency domain stress-strain relationship $\tilde{\sigma}(\omega)$–$\tilde{\varepsilon}(\omega)$ results in

$$\tilde{\sigma}(\omega) = E^*(\omega)\tilde{\varepsilon}(\omega) \tag{3}$$

where the complex modulus $E^*(\omega)$ can be written as

$$E^*(\omega) = E^{'}(\omega) + \mathrm{i}E^{''}(\omega) = E^{'}(\omega)[1 + \mathrm{i}\eta(\omega)] \tag{4}$$

$E^{'}(\omega)$ is the storage modulus, $E^{''}(\omega)$ is the loss modulus, and $\eta(\omega)$ is the loss factor calculated as

$$\eta(\omega) = \frac{E^{''}(\omega)}{E^{'}(\omega)} \tag{5}$$

The complex modulus $E^*(\omega)$ behavior is influenced by multiple factors (excitation conditions, amplitude, frequency, temperature, prestress, relative humidity, and among others) where temperature, frequency, and amplitude are the most relevant ones [9]. Involving the frequency

influence, the ASTM E 756–04 "standard test method for measuring vibration-damping properties of materials" [10] details the methodology needed to characterize the mechanical behavior of nonself-supporting viscoelastic materials in the frequency range of 50–5 kHz, implying the use of multimaterial Oberst beam specimens. Nevertheless, the main inconvenience of ASTM E 756–04 standard consists in introducing additional damping or mass through the excitation or through the measurement devices. Many authors investigated these inconveniences [11], which lead to generate alternative methods with improved accuracy [12–20]. Others techniques based on forced vibrations as the Weissenberg rheogoniometer [21], the dynamic mechanical analysis (DMA) technique [22], and the dynamic mechanical thermal analysis (DMTA) technique have also been implemented [23].

In particular, DMTA technique considers together time and temperature by applying the superposition (TTS) principle [24]. The superposition principle relates the material response at a given time t and at a given temperature T under different conditions assuming a relation

$$E(t,T) = E(t_0, \alpha_T T_0) \tag{6}$$

where T and T_0 represent the reference temperature and the reference time, respectively, and α_T is the shift factor relating T to T_0. Accordingly, this principle can also be applied to frequency domain by means of

$$E^*(f,T) = E^*(f_0, \alpha_T T_0) \tag{7}$$

where f and f_0 represent the frequency to be shifted and the reference one, respectively, whereas the shift factor α_T relates f to f_0 in the frequency domain. Arrhenius and William-Landel-Ferry (WLF) [25] are the commonly applied models, where the former model is given by

$$\log\alpha_T = C\left[\frac{1}{T} - \frac{1}{T_0}\right] \tag{8}$$

where C is a constant, the William-Landel-Ferry model can be expressed by

$$\log\alpha_T = \frac{-C_1\Delta T}{C_2 + \Delta T} \tag{9}$$

where C_1 and C_2 are constants and $\Delta T = T - T_0$.

Hence, if the objective is to describe the material behavior in frequency or temperature ranges outside of the tested ones [25], the TTS principle can be used to derive the master curves (MC).

It should be noted that to apply DMTA techniques for characterizing viscoelastic materials, defect free adhesive specimens are required. The required quality of the specimens can be obtained by applying nondestructive evaluation (NDE) techniques (such as ultrasonic, acoustic emission, radiography, thermography, shearography, holography, and vibration analysis [26], the neutron radiography and the ultrasonic scan [27, 28]). Through these NDE techniques allow the detection of voids such as cracks or other regions of uncured adhesive [29–33]. Most

of the research studies [31–33] are focused on the NDE of adhesive joints, but pay attention to adhesion failures.

As a resume, the experimental characterization of the material response to both time and frequency domain is described and also focusedon the specimen preparation and validation. Therefore, the objective of this research is to characterize, under tension strain, the relaxation and the dynamic behavior of the flexible adhesive ISR 70-03:

- The materials and the experimental techniques employed are presented.
- The influence of the strain level and test specimen thickness into specimen behavior is analyzed.
- Relaxation and dynamic master curves are developed using the time-temperature superposition principle. Related shift factors α_T are fitted to the Arrhenius model (Eq. (8)).
- The constructed master curves are fitted to a generalized Maxwell and to a fractional derivative model.

Hence, the proposed models are capable of describing the influence of time, temperature, and strain level over the mechanical properties of the flexible adhesive ISR 70-03.

2.1. Experiments

The mechanical behavior of the analyzed material was characterized by means of relaxation and dynamic tests at different temperatures. A DMTA equipment (RSA3 of TA Instruments) equipped with climate chamber, the Faculty of Engineering of the University of Oviedo, was employed.

2.1.1. Materials and experiments

The studied flexible adhesive is modified silane, commercially named ISR 70-03 produced by Bostik. Regarding the test specimens that were obtained from plates of the cured adhesive produced using casts of 50 × 70 mm × h, where h is the nominal thickness. Three casts with different thickness h of 0.5 mm, 1.0 and 1.5 mm were manufactured. They were manufactured using Teflon to guarantee that a plate of solid material can be demoldedwithout degradation after the curing. The cure time was 48 h for all plates; at room temperature no specific equipment was employed [34]. Consequently, the proposed procedure can be outlines as follows:

- First, the nozzle is drawn along the length of the cast in a zig-zag motion without removing the tip. It should be empathized that the nozzle does not touch with the cast surface in order to ensure an adequate lower surface finish for the adhesive plate.
- Second, when enough amount of adhesive is spread, it is forced to fill the cast, in a single uniform motion by means of a spatula made of Teflon. The spatula has round corners in order to obtain a uniform upper surface finish.

No chemical products are used to prepare the specimens. From the uniform obtained plates, rectangular specimens were cut and measured using an optical microscope. The obtained width and thickness values of each sample are presented in **Table 1**.

Identification sample	Width (mm)	Thickness (mm)
P1	5.45	1.38
P2	5.94	1.50
P3	6.58	1.47
P4	5.26	0.85
P5	6.24	0.78
P6	6.21	0.92
P7	5.25	0.75
P8	5.91	0.45
P9	5.66	0.48
P10	5.69	0.47

Table 1. Specimen dimensions.

To ensure the quality of the produced specimens, tomography techniques by means of neutron radiographies were used. Two defects were found: internal voids and superficial flaws. Accordingly, defect-free samples were identified and selected for testing and denoted as P1, P3, P6, and P10. **Figure 1** shows some of the manufactured samples with defects (P2 and P9) and without (P6 and P10), respectively.

Finally, a DSC test (see Ref. [35] for details) was carried out to determine the glass transition temperature, $T_g = -64°C$.

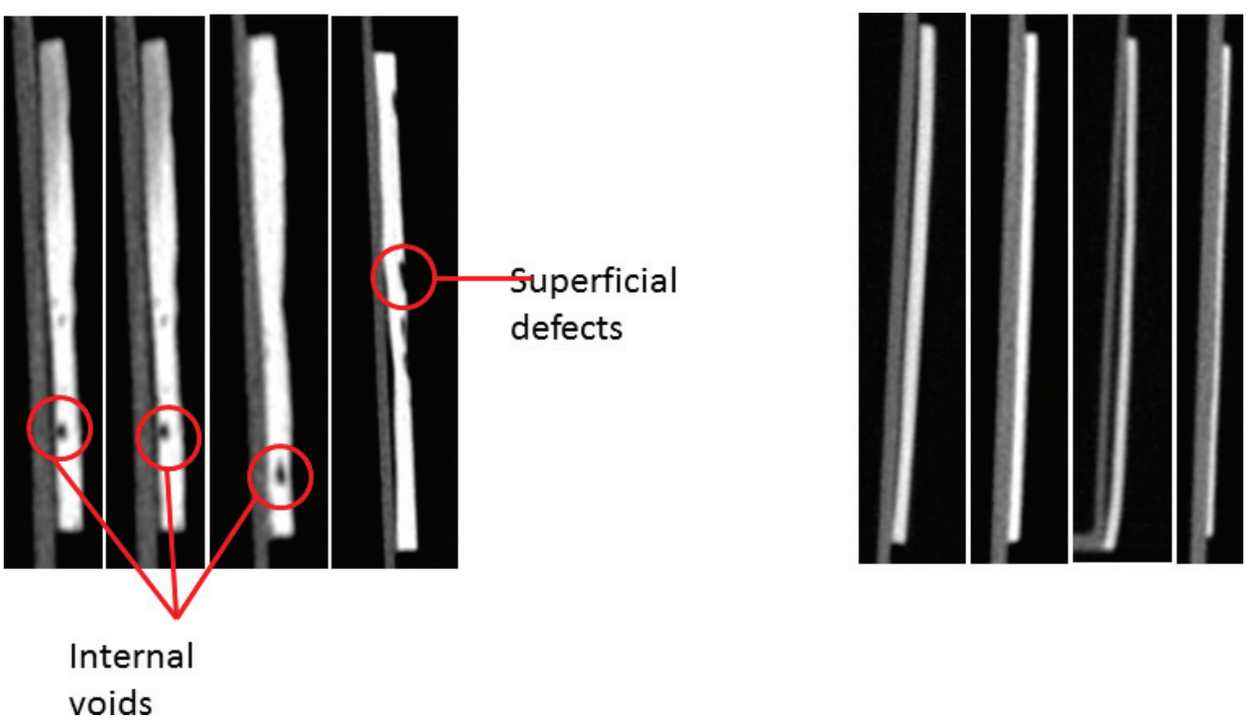

Figure 1. Tomography analysis: specimens with defects, defect-free specimens.

2.1.2. DMTA test

The specimens were studied using a tensile fitting tool shown in **Figure 2**. For the relaxation and dynamic tests, the specimens were prestressed to avoid the buckling effect of tightening the tool screws. Hence, it was verified that the measured force was higher than the prestress at any time all over the experiments. Under these conditions, two different tests were performed in the RSA3 DMTA. First, linearity was studied and second the experiments to obtain the material master curve (MC) were performed. In the latter group, the equipment climate chamber was used and the stabilization time at each temperature was about 10–15 min. These master curves represent the relation between the stress and the strain. Therefore, the relaxation master curve represents the relaxation modulus $E(t)$ while the dynamic one represents the complex modulus $E^*(\omega)$.

Concerning the linearity, the tests were performed at a reference temperature of 20°C. Both specimen thickness and the strain level parameters were analyzed:

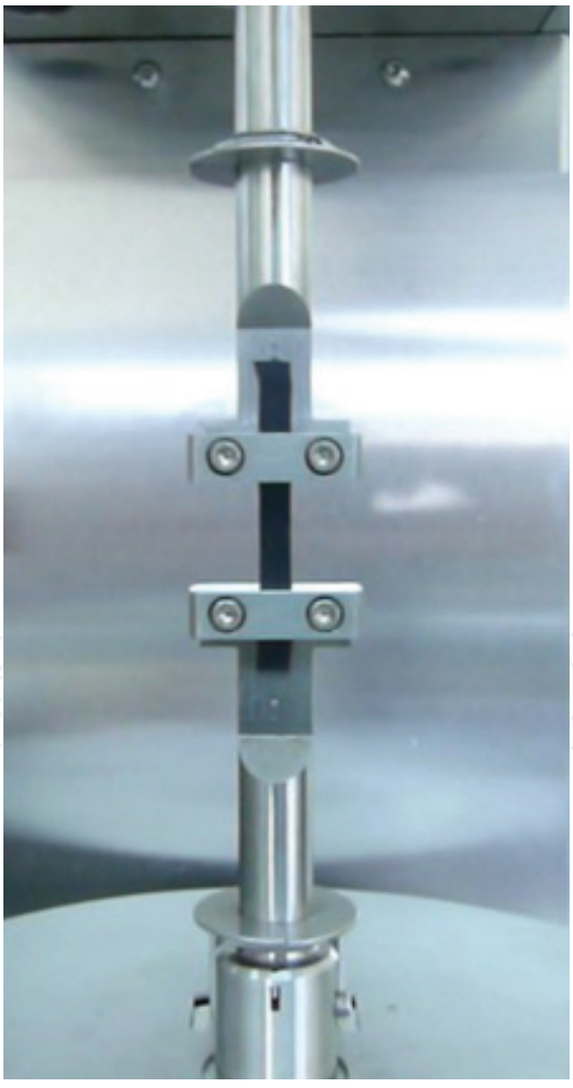

Figure 2. Detail of tension supporting tool.

First, relaxation tests were performed using three samples (P3, P6, and P10) with dimensions shown in **Table 1**. Two test series differing in the induced strain level were completed. Strain levels of $\varepsilon = 0.5$ and $\varepsilon = 2\%$ were, respectively, applied in a time range of 10^{-2} s–10^{2} s.

Following, seven relaxation tests were carried out using only the specimen P1 (see **Table 1**). In these tests, the analyzed time range was 10^{-2} s–4×10^{3} s for induced strain levels of $\varepsilon = 0.2$, $\varepsilon = 0.5$, $\varepsilon = 1$, $\varepsilon = 2$, $\varepsilon = 5$, $\varepsilon = 7$, and $\varepsilon = 8\%$.

For the MC, relaxation and dynamic tests were conducted over sample P3. In both cases, the strain level induced was 0.5%. For the relaxation MC, the analyzed temperature range was −40 to 50°C, where 10 different relaxation tests were carried out. For the dynamic MC, the temperature range was −10 to 20°C and four tests were deformed.

2.2. Results and discussion

2.2.1. Linearity analysis of the adhesive behavior

Next, the linearity regarding the material behavior is analyzed involving two test conditions, sample thickness and strain level influence, both by means of relaxation tests.

First, the thickness influence is studied. **Figure 3** shows relaxation test series for $\varepsilon = 0.5\%$ and **Figure 4** shows relaxation test series for $\varepsilon = 2\%$.

From **Figures 3** and **4**, it should be remarked that the relaxation modulus $E(t)$ for the thickness $h = 1.5$ mm is slightly higher than the others, anyway less than 5% in both cases. Considering that the results were derived from different specimens, certain dispersion between the obtained relaxation modulus $E(t)$ can be expected. Therefore, it can be concluded that the specimen thickness has a negligible influence on these test results.

Next, the strain influence on the range of $0.2\% < \varepsilon < 8\%$ over the relaxation modulus $E(t)$ is analyzed through seven tests. The results are illustrated in **Figure 5**.

From **Figure 5**, it can be noted that the $\varepsilon = 0.2\%$ and $\varepsilon = 0.5\%$ curves show slight fluctuations that are not visible for the other curves. These inaccuracies can be expected with the strain decrement, because the force may be lesser than the machine resolution. Consequently, as the strain increases, this effect is less significant. Hence, only the curve $\varepsilon = 0.2\%$ could be rejected due to the fluctuations.

Figure 5 shows that the adhesive material behavior depends on the imposed strain level where the higher the strain, the lower the experimental relaxation modulus $E(t)$. This implies that the material softens when the strain level grows up. With the aim of comparing the relaxation moduli $E(t)$ obtained for the different strain levels, **Figure 6** shows the corresponding ratios taking $\varepsilon = 0.5\%$ as a reference.

Assuming inherent scatter (see **Figure 6**), a nearly constant $E(t)$ratio can be verified for the range of strains analyzed, even for $\varepsilon = 0.2\%$. Consequently, the strain influence on the relaxation modulus can be modeled using Eq. (10)

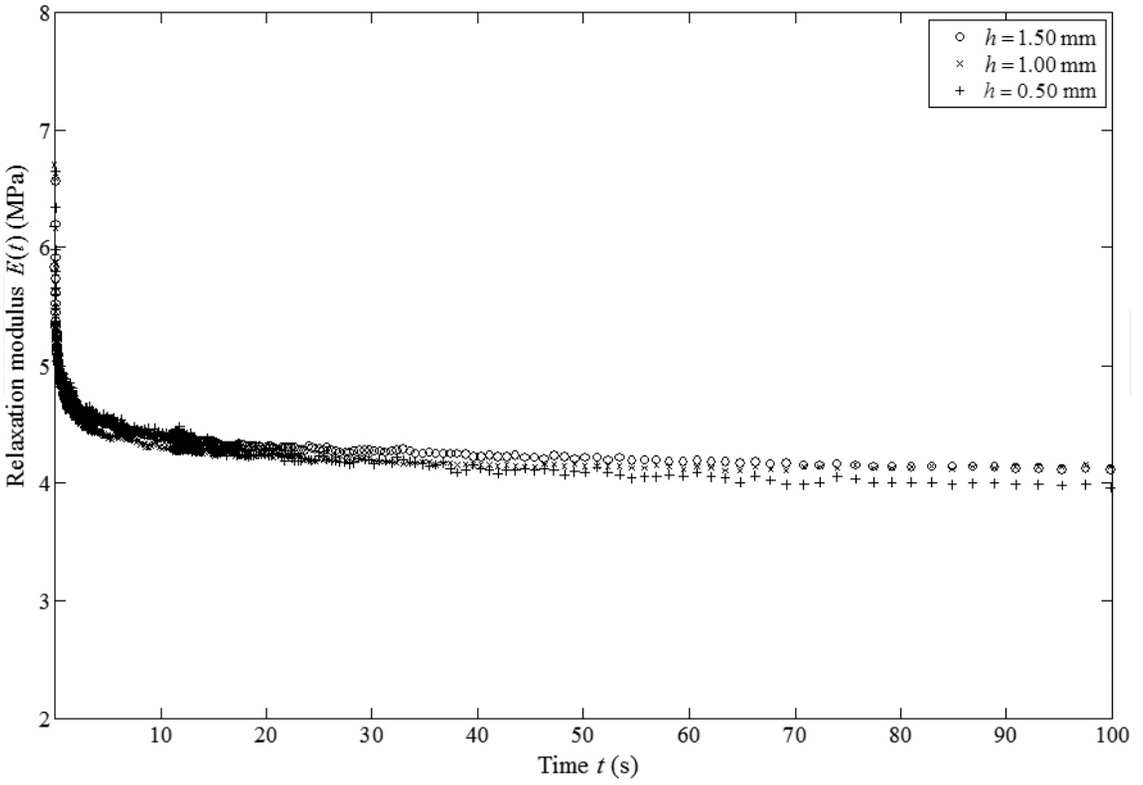

Figure 3. Relaxation modulus tests for thickness influence evaluation for $\varepsilon = 0.5\%$.

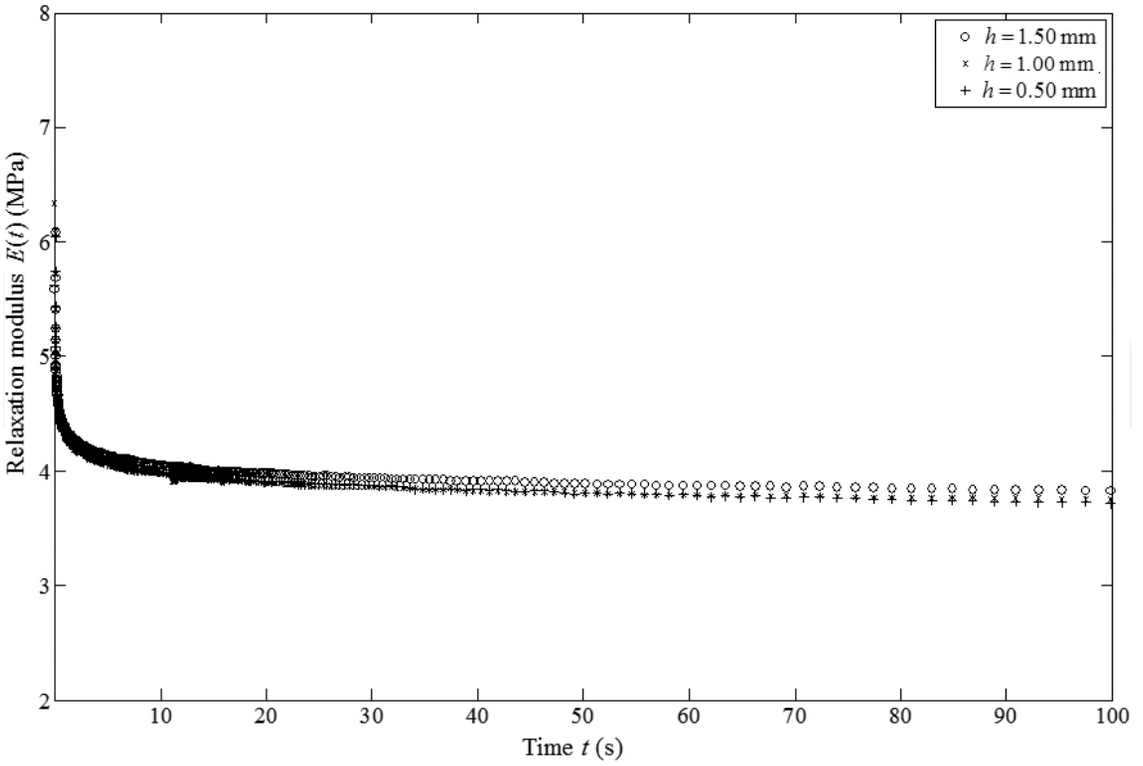

Figure 4. Relaxation modulus tests for thickness influence evaluation for $\varepsilon = 0.5\%$.

http://dx.doi.org/10.5772/66104

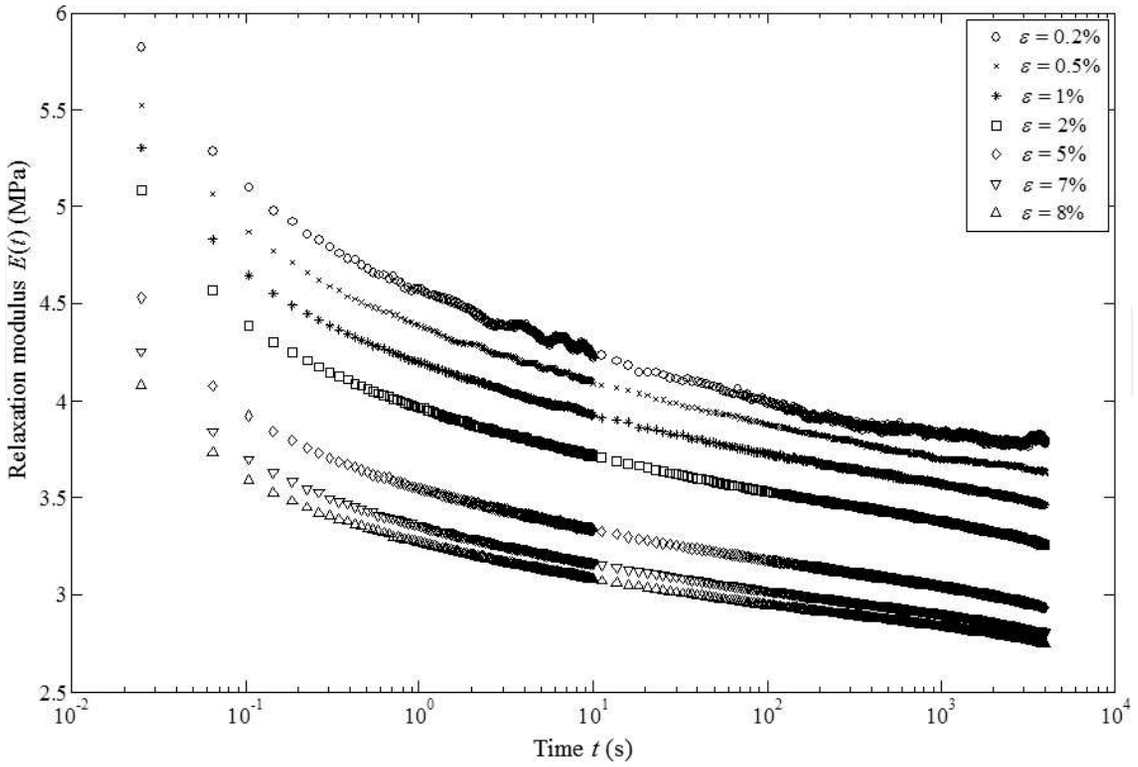

Figure 5. Relaxation modulus tests for strain influence evaluation.

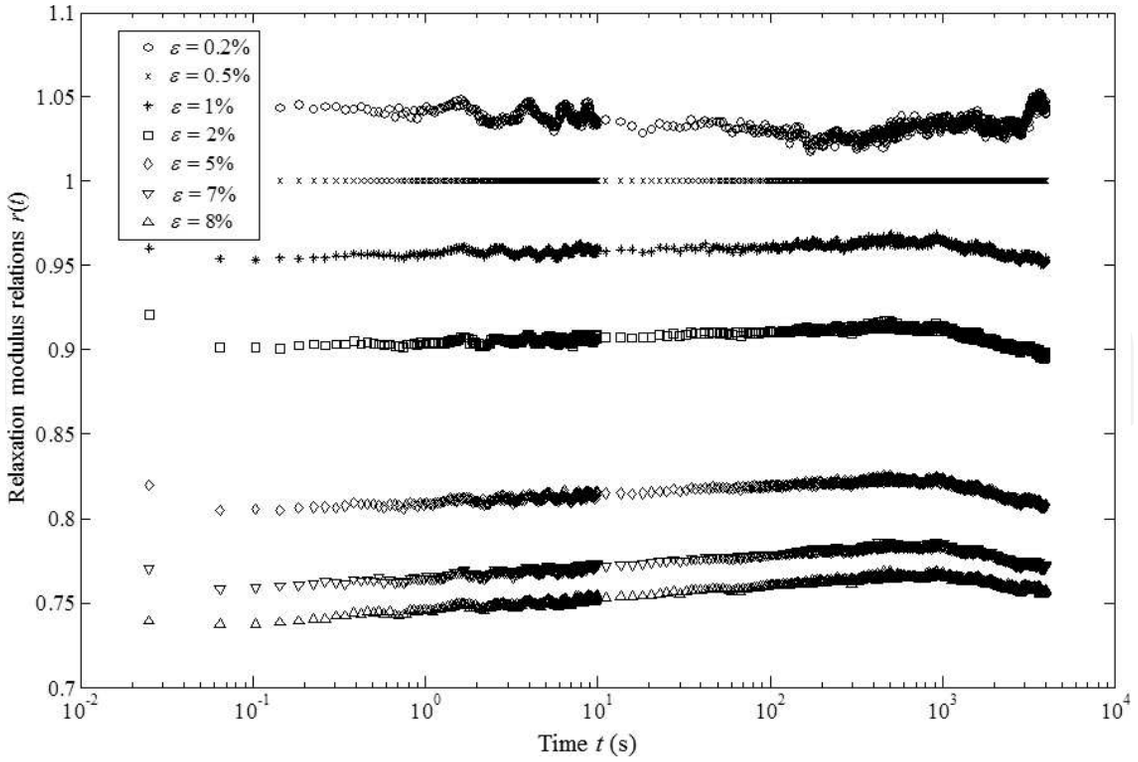

Figure 6. Ratio of relaxation moduli $r(t)$ for $\varepsilon = 0.5\%$ as a reference.

$$E(\varepsilon, t) = r(\varepsilon) \times E_{\text{ref}}(t) \tag{10}$$

where $r(\varepsilon)$ is the ratio between the relaxation modulus $E(\varepsilon, t)$ for the strain ε and that taken as a reference $E_{\text{ref}}(t)$. In this context, **Figure 7** shows the evolution of the mean value of the ratio $r(\varepsilon)$ of different strains as a function of the strain ratio, taking $\varepsilon_{\text{ref}} = 0.5\%$ as a reference.

The decay of the mean value of these ratios with the strain presented in **Figure 7** can be fitted by an experimental function according to

$$r(\varepsilon) = \gamma_1 + \gamma_2 \mathrm{e}^{-\gamma_3 \frac{\varepsilon}{\varepsilon_{\text{ref}}}} \tag{11}$$

where the parameters γ_1, γ_2, and γ_3 were estimated by least squares, as $\gamma_1 = 0.73780$, $\gamma_2 = 0.30504$, and $\gamma_3 = 0.14792$, and where ε_0 represents the reference strain level, being $\varepsilon_{\text{ref}} = 0.5\%$ for the present cases. The function $r(\varepsilon)$ of Eq. (11) is represented in **Figure 7** by the discontinuous trace.

In order to verify the proposed model, the results provided by Eqs. (10) and (11) are compared with the experimental data obtained for the strain $\varepsilon = 2\%$, and as **Figure 8** illustrates, Eqs. (10) and (11) provide an accurate prediction of the material relaxation in the 10^{-2} s–4×10^3 s range of time.

Based on the results, it can be observed that mechanical properties of the flexible adhesive ISR 70-03 do not depend on sample thickness. In contrast, they do depend on the strain level. Thus,

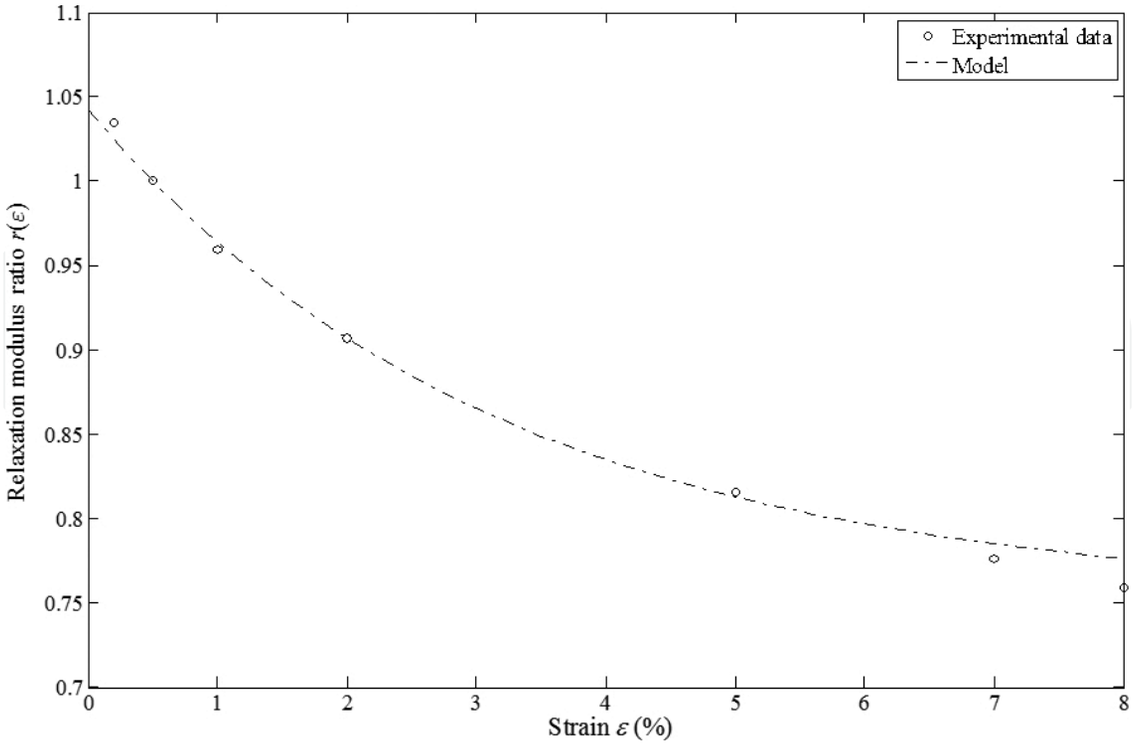

Figure 7. Ratio of the relaxation modulus relations $r(\varepsilon)$ by Eq. (11).

http://dx.doi.org/10.5772/66104

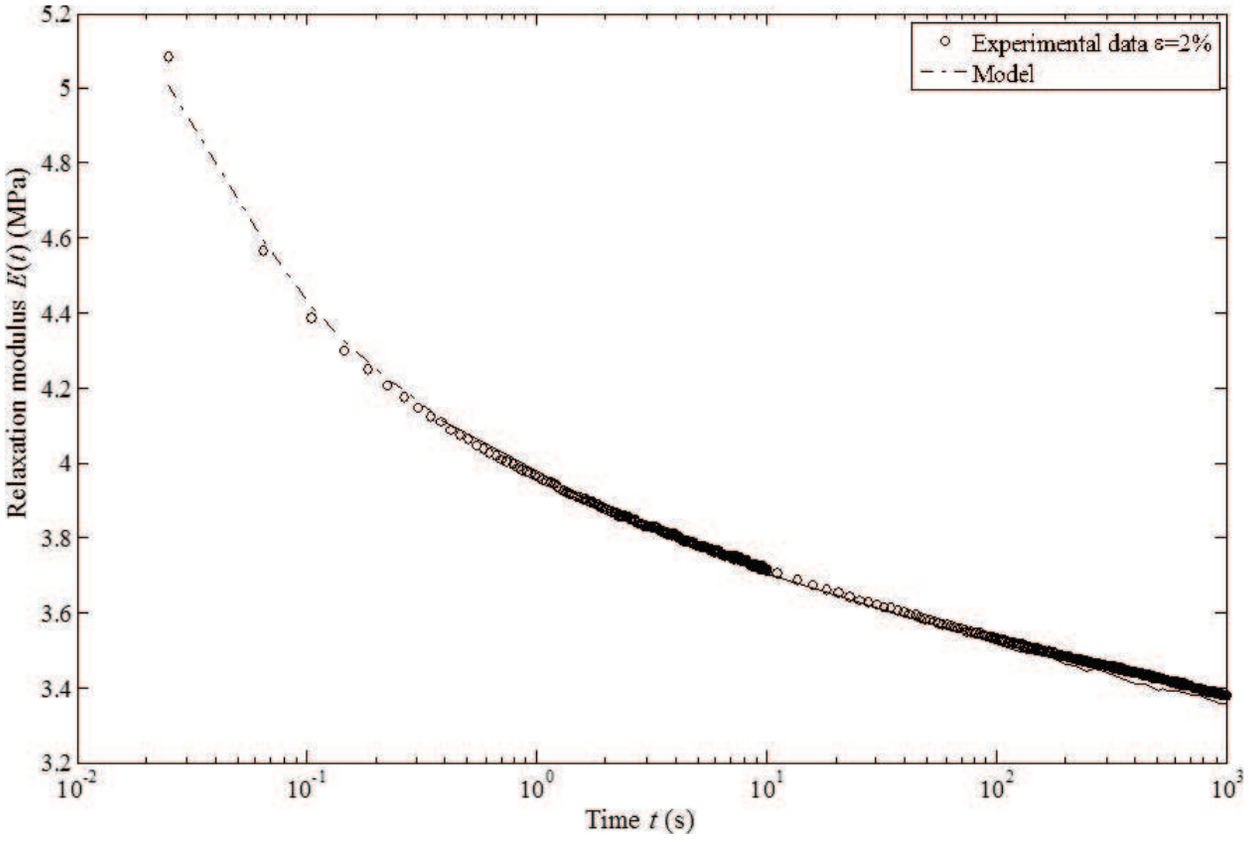

Figure 8. Relaxation modulus given by Eq. (**10**).

the lower the strain, the higher the relaxation modulus, leading to the conclusion that the material softens as the strain level grows up. Consequently, the exponential model given by Eq. (11) represents the influence of the strain level and Eq. (10) allows computing the relaxation modulus function $E(t)$ for any strain level, once the relaxation modulus for a reference strain level is obtained.

This increase in the relaxation modulus $E(t)$ as a consequence of the decrease in the strain level is in accordance to the observed behavior in other viscoelastic materials [36] so as other rubber like compounds [37] used for vibration control.

2.2.2. Relaxation master curve

Following, the time domain master curve (MC) is obtained applying the time-temperature superposition (TTS) principle [25]. The MC is built-up from 10 relaxation curves, obtained for 10 different temperatures ranging from −40°C–50 °C all of them in the 10^{-2} s–10^{2} s range, as shown in **Figure 9**.

From **Figure 9**, it should be remarked that the higher the temperature, the lower the relaxation modulus. It should be noted also that the test carried out at $T = 30°C$ intersects the one at $T = -20°C$ due to an error during the test. Analogous situation can be verified for the curves$T = -10°C$ and $T = -20°C$. Reasons for removing these curves from the analysis will be discussedlater.

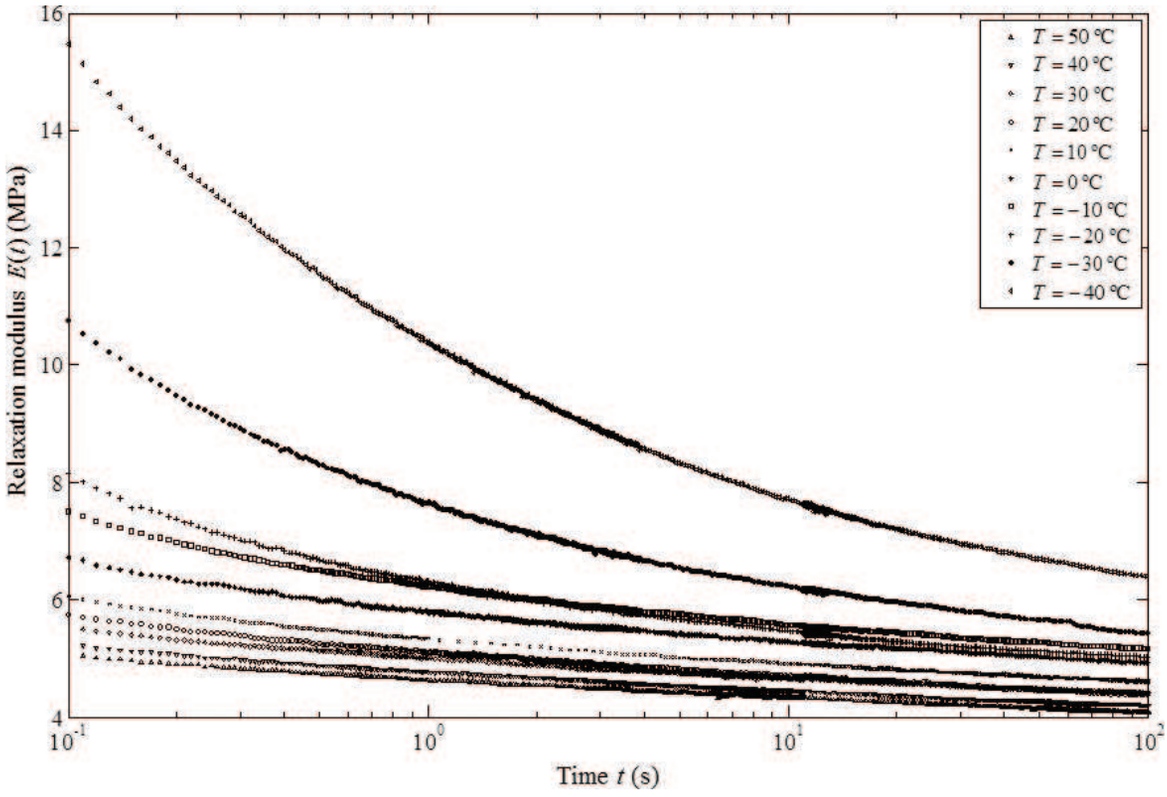

Figure 9. Relaxation curves resulting from a broad range of temperatures.

Based on the industrial application, the temperature $T_0 = 20°C$ is chosen as a reference to derive the MC. First, all the possible shift factors $\alpha_T(t_0)$ between the reference curve and that for $T = 10°C$ are computed. Thereafter, the times t and t_0 are determined for which the relaxation modulus curves coincide, $E(t, 10°C) = E(t_0, 20°C)$. Accordingly, the shift factor $\alpha_T(t_0)$ at any time t_0 is computed as

$$\alpha_T(t_0) = t/t_0. \tag{12}$$

Based on the TTS principle, singe shift factor α_T should exist for each temperature. Therefore, the optimum shift factor $\alpha_T(t_0)$ is computed from all the possible factors. This is done by minimizing the error function defined as the difference between the original and the shifted curves. Then, a preliminary MC is reached, for which the procedure is repeated for any curve represented in **Figure 9**.

Figures 10 and **11** show the range of possible factors $\alpha_T(t_0)$ obtained from each preliminary MC and the one to be shifted below and above $T_0 = 20°C$, respectively.

From **Figures 10** and **11**, significant conclusions can be obtained. Involving the curves for temperatures $T = -40, -20, -10, 0, 10, 40,$ and $50°C$ nearly constant $\alpha_T(t_0)$ factors are computed in accordance to the TTS principle. Hence, a reasonable optimum value can be determined at each temperature. On the contrary, the curve for $T = -30°C$ exhibits high scatter and should, therefore, be disregarded from the analysis.

http://dx.doi.org/10.5772/66104

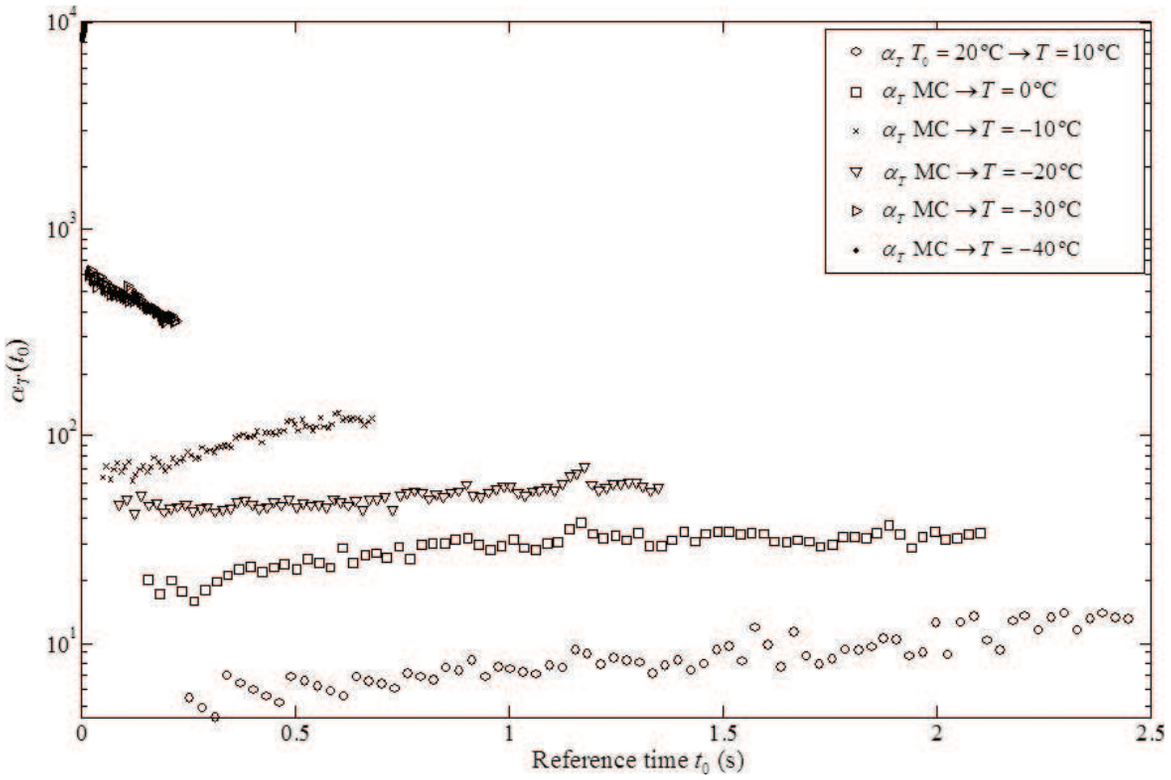

Figure 10. Range of possible factors $\alpha_T(t_0)$ in time domain below T_0.

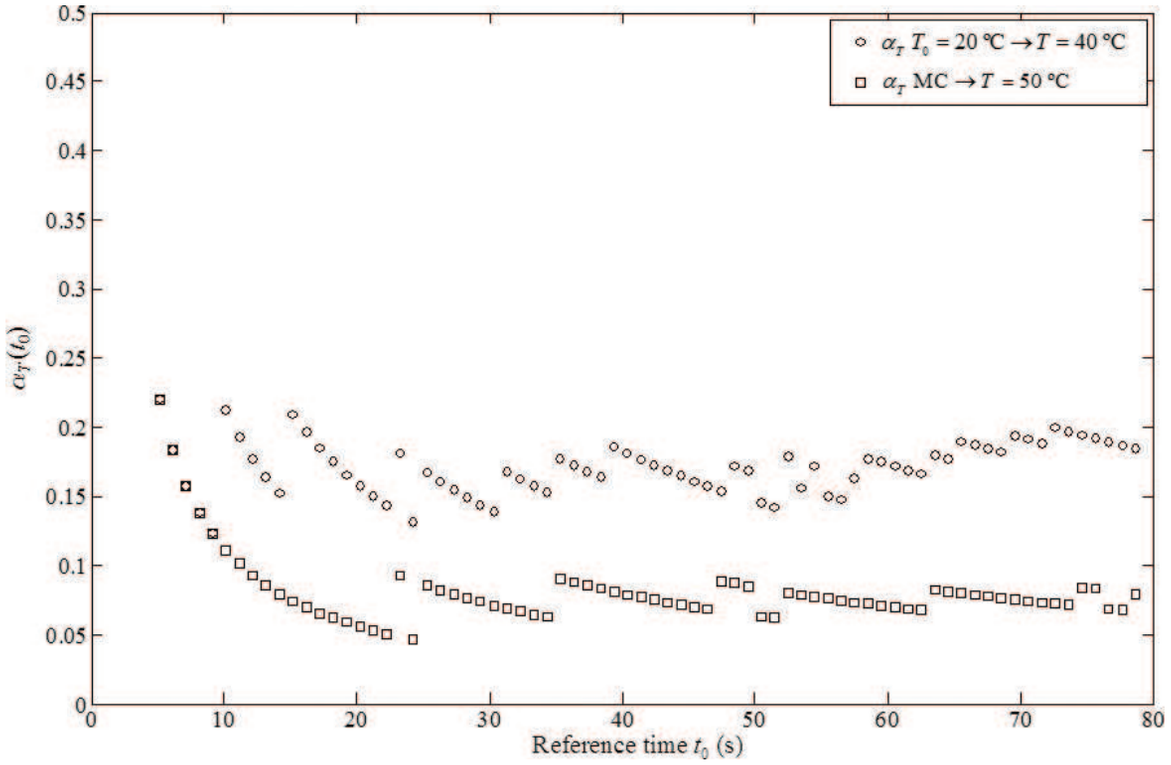

Figure 11. Range of possible factors $\alpha_T(t_0)$ in time domain above T_0.

It should be mentioned that the position for the curves resulting for $T = -10$ °C is shifted and, therefore, at least one of them must be removed from the analysis. Decision is taken based on the optimum shift factors α_T represented as a function of temperature in **Figure 12**.

It follows from **Figure 12** that, in order to obtain a monotonically decreasing $\log\alpha_T - T$ curve without irregularities, it is convenient to discard the information provided for $T = -20$°C. The observed behavior can be modelized using the Arrhenius model (Eq. (8)), the results of which is represented in **Figure 12** by the discontinuous trace. The parameter C was estimated by linear regression, giving $C = 4419$ K, corresponding to a regression coefficient $R^2 = 0.999$.

Therefore, applying the presented procedure and computing the optimums α_T values shown in **Figure 12**, each single curve has been shifted to built-up the desired relaxation master curve, as shown in **Figure 11**. The constructed MC decays from 16 MPa down to 4 MPa in the covered range 10^{-5} s–1.6×10^3 s.

Based on the results, it can be said that the studied material can be used for vibration control proposes. It should be remarked also that based on the mechanical strength, the ISR 70-03 can be employed not only for non-structural applications but also more demanding structural designs that can be proposed [38, 39].

2.2.3. Dynamic master curve

The dynamic MC can be constructed using an analogous procedure to that followed in the derivation of the master curve for the relaxation modulus. Hence, **Figure 12** represents four

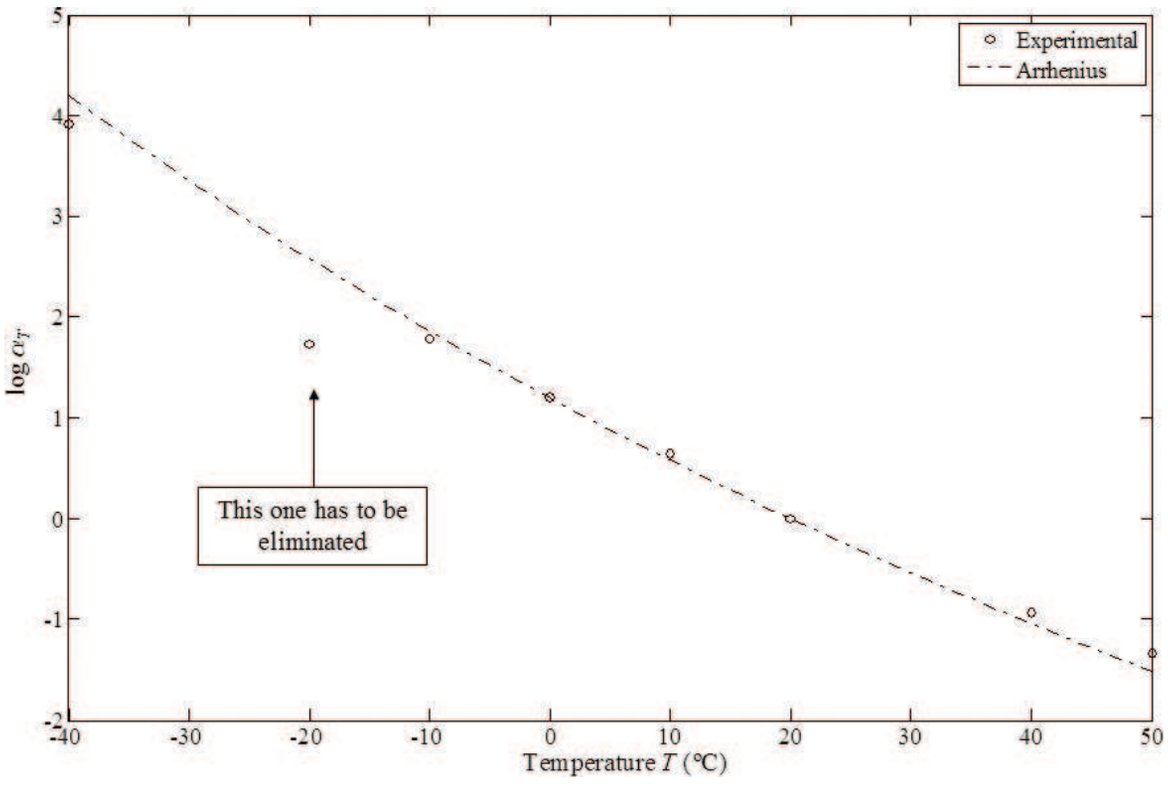

Figure 12. Optimum shift factor α_T values for time domain and Arrhenius model fit.

http://dx.doi.org/10.5772/66104

curves of the storage modulus $E^{'}$ and loss factor η, respectively, in the 10^{-1} Hz–2×10^{1} Hz frequency range, for four different temperatures, $T = -10, 0, 10,$ and 20°C. In this case, taking as well into account the industrial application, the same reference temperature $T_0 = 20$°C has been adopted.

Figure 13 shows that the higher the temperature, the lower both the storage modulus $E^{'}$ and the loss factor η. Obviously, this in accordance with the results obtained in the time-domain case.

Therefore, all the possible shift factors $\alpha_T(f_0)$ between the preliminary master curve and the one to be shifted are computed using the storage modulus $E^{'}(f,T) = E^{'}(f_0, T_0)$, and the shift factors $\alpha_T(f_0)$. Thus, the shift factor $\alpha_T(f_0)$ represented in **Figure 14** satisfying

$$\alpha_T(f_0) = f/f_0. \tag{13}$$

Taking into account the moderate scatter in the results assignable to the experimental nature of the data, the $\alpha_T(f_0)$ values of the three curves shown in **Figure 15** may be taken as a constant. To compute a single value for each temperature, an analogous minimization procedure to that followed in the relaxation case was applied to the complex modulus $E^{*}(f,T)$. The resulting optimums shift factors α_T are computed and represented in **Figure 16**.

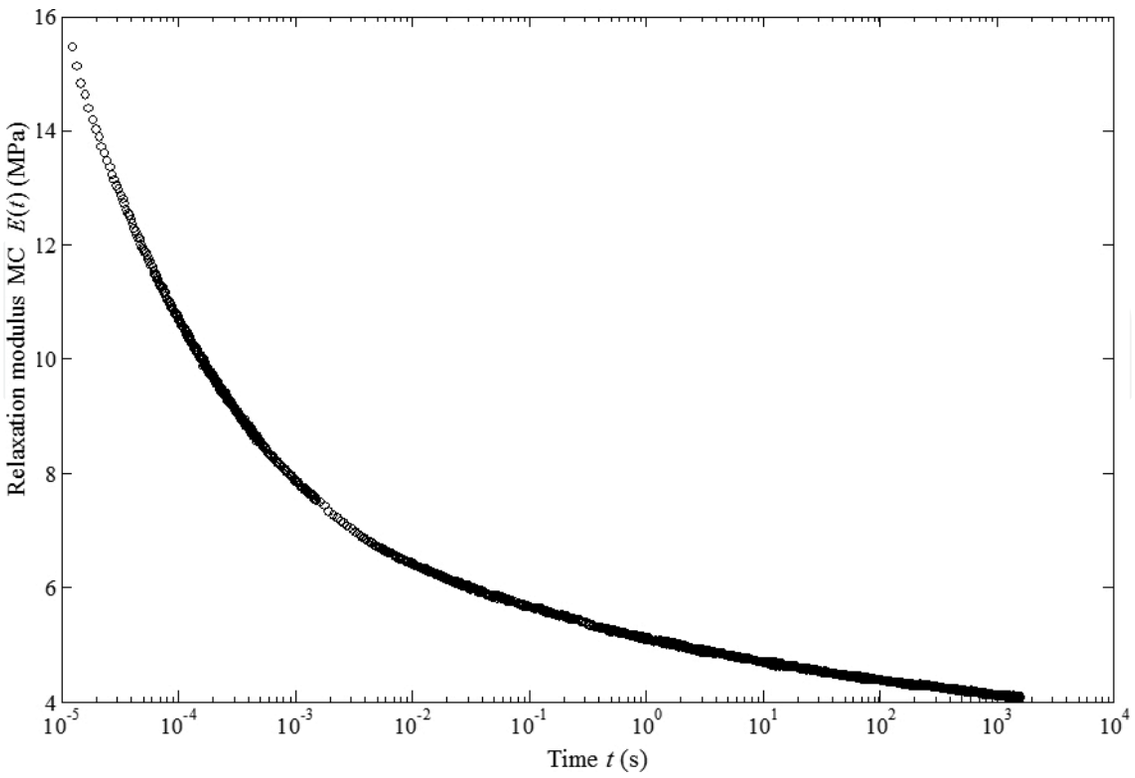

Figure 13. Storage modulus and loss factor curves for four different temperatures.

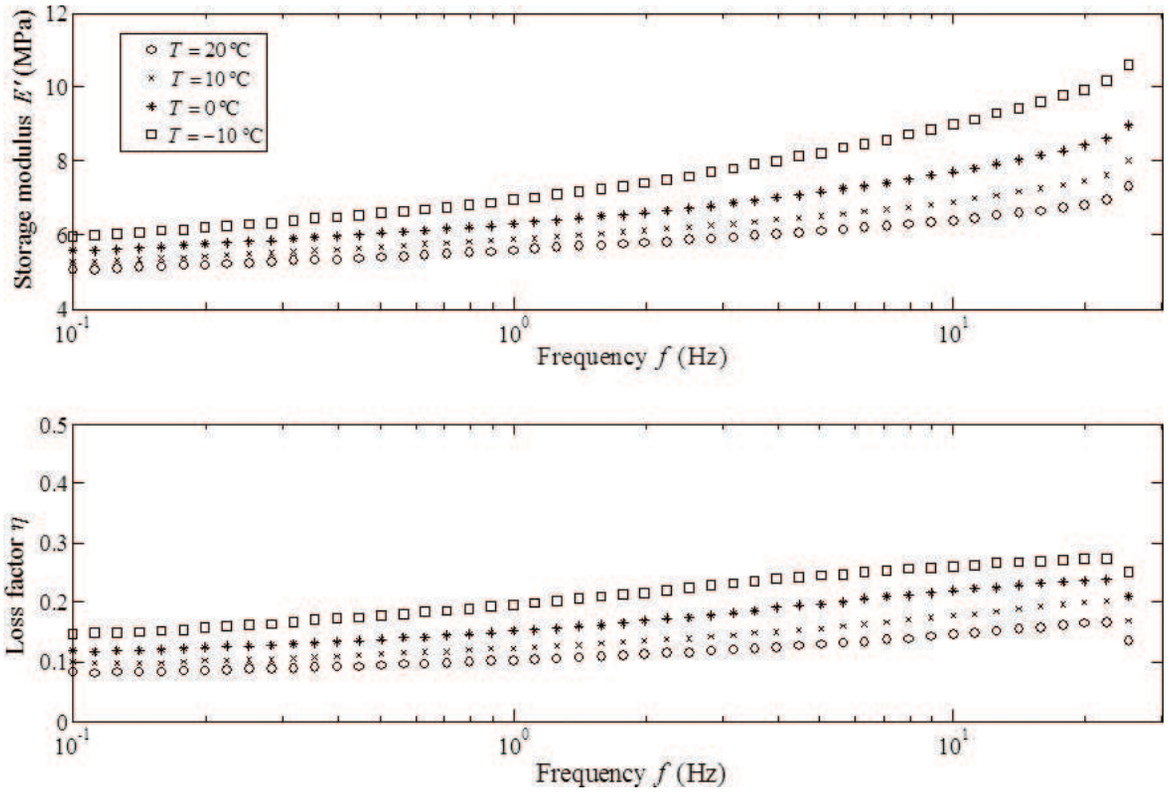

Figure 14. Relaxation master curve in time domain.

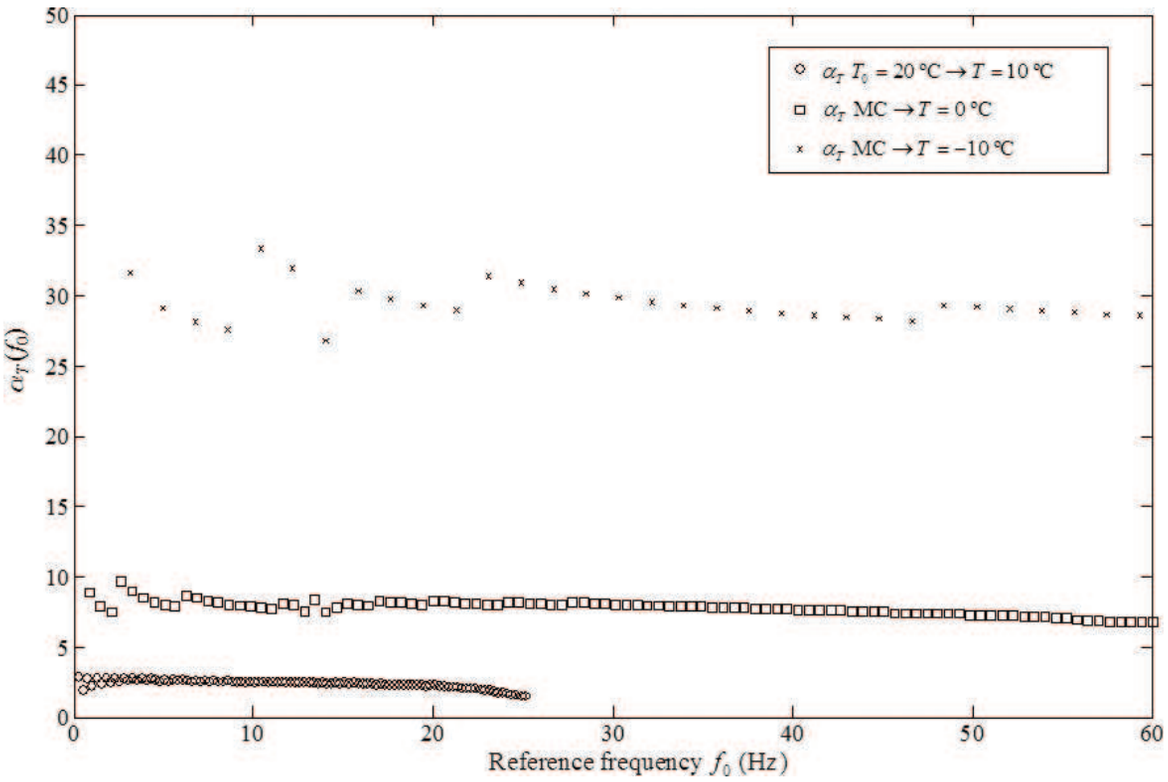

Figure 15. Shift factors $\alpha_T(f_0)$ in frequency domain below T_0.

http://dx.doi.org/10.5772/66104

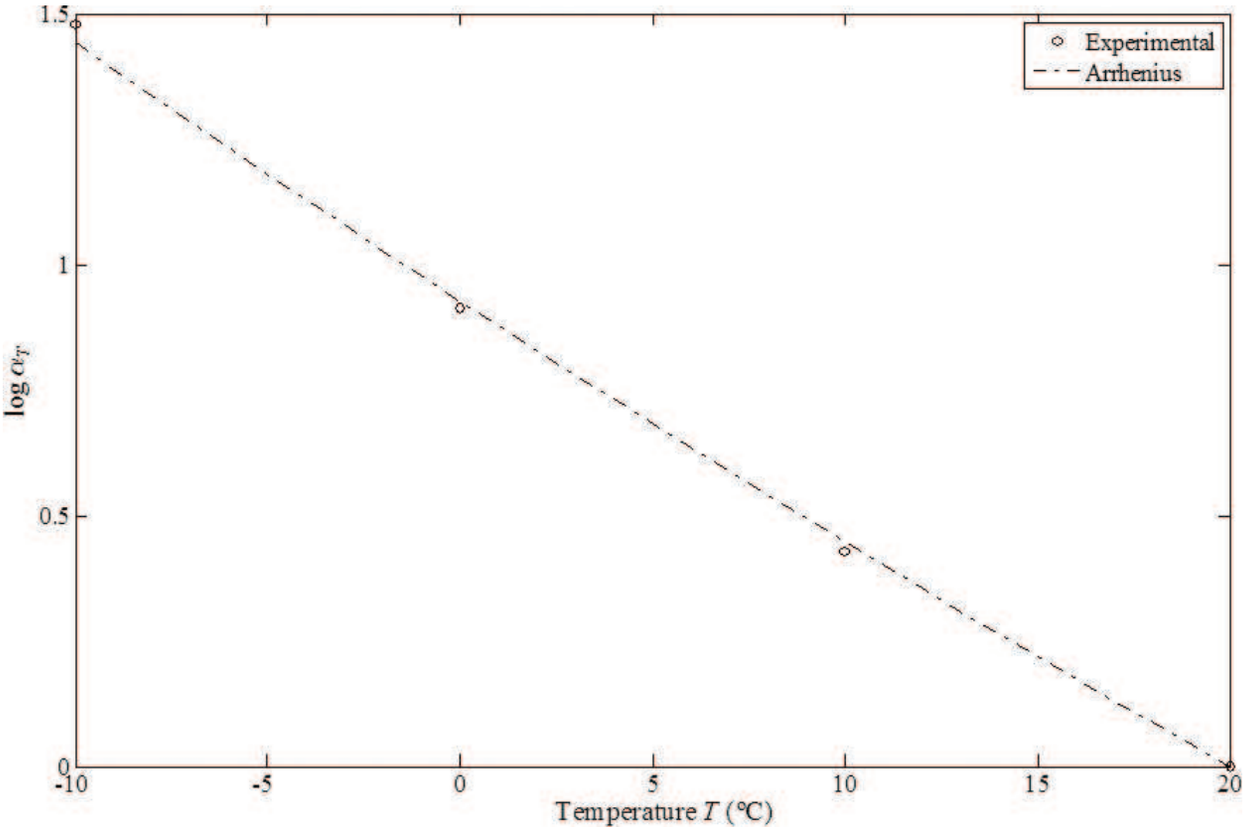

Figure 16. Optimum shift factor a_T values for frequency domain and Arrhenius model fit.

It can be seen from **Figure 16** that the determinedvalues decay with the temperature. Similarly as in the time-domain case, it follows that the Arrhenius model (Eq. (8)), which is represented in **Figure 13** by the discontinuous trace, is a good candidate for describing the dynamic behaviorobserved in the material. The parameter C became $C = 3710$ K for a regression coefficient $R^2 = 0.999$. Consequently, the corresponding MC is constructed as shown in **Figure 17**.

In **Figure 17** the MCs for the storage modulus $E^{'}$ and loss factor η in the range 0.1 Hz–700 Hz are illustrated where the rubbery behavior and the beginning of the transition zone are present. As it was concluded in the time-domain analysis, the ISR 70-03 is applicable for vibroacoustic control of structures even for low frequency applications [36].

2.3. Models

Next, a relaxation modulus model capable of taking into account together the influence of strain, time and temperature as

$$E(\varepsilon, t, T) = r(\varepsilon) \times E_{\text{ref}}(t, T). \tag{14}$$

is proposed. Concretely, a generalized Maxwell model (also known as the Prony series model) [40] and a fractional model [41] are fitted to the previously obtained master curve $E_{\text{ref}}(t)$, in the

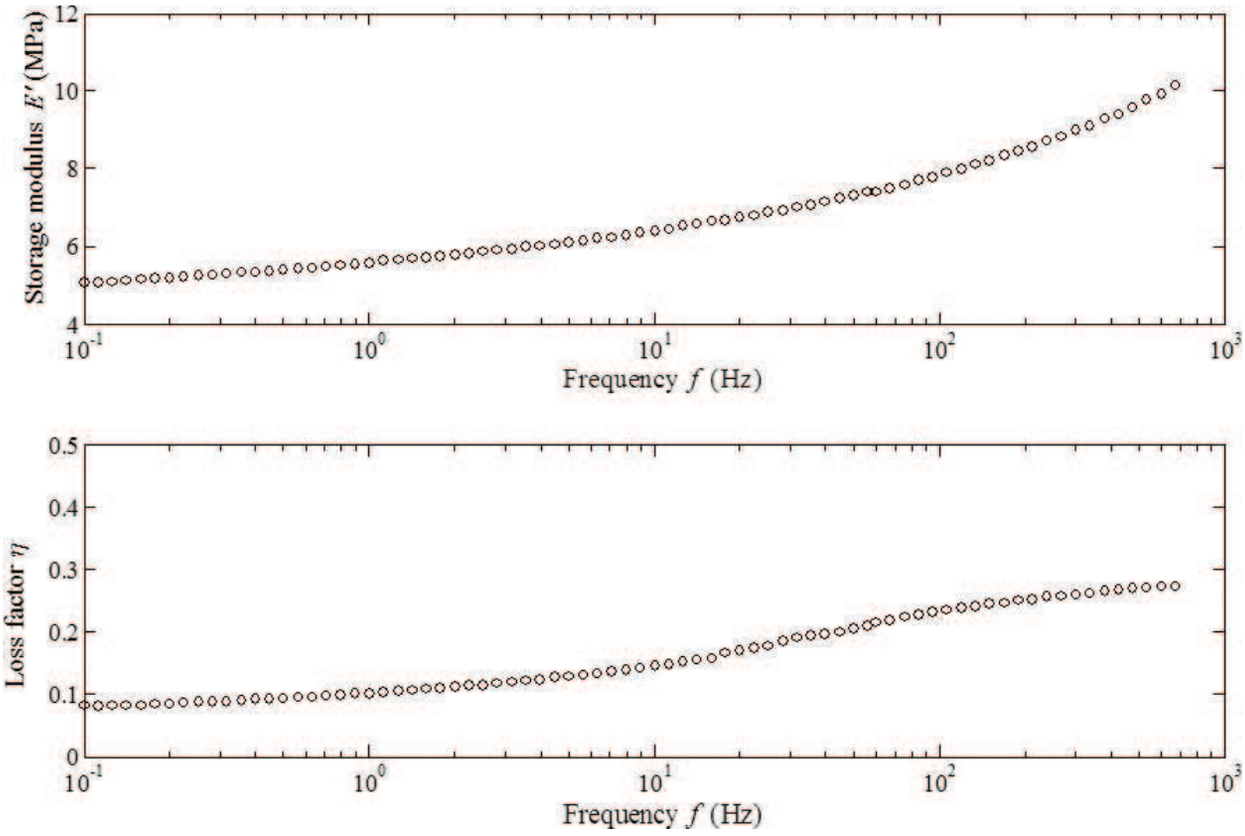

Figure 17. Master curves for the storage modulus and loss factor in frequency domain.

time range of 1×10^{-5} s–1.6×10^{3} s. Also, a complex modulus model is suggested to modelize the dynamic master curve $E^*(f)$ in the frequency range of 0.1 –700 Hz.

2.3.1. Relaxation models

Next, two relaxation models are presented. Concerning the generalized Maxwell (or Prony series) model, $E_{\text{ref}}(t)$ yields

$$E_{\text{ref}}(t) = E_0 + \sum_{i=1}^{N} E_i \mathrm{e}^{-t/\tau_i}. \tag{15}$$

where E_0 is the relaxed modulus, E_i represents stiffness parameter and τ_i denotes relaxation time. $N = 9$ is the number of terms chosen for the generalized Maxwell model to accurately represent the experimental results. The fitting has been carried out by least squares, corresponding to a regression coefficient of $R^2 = 0.999$. The obtained values for E_0, E_i and τ_i are presented in **Table 2**.

Concerning the fractional derivative model, the four-parameter derivative model [42]

$$\sigma(t) + \tau^{\alpha}\mathrm{D}^{\alpha}\sigma(t) = E_{\mathrm{r}}\varepsilon(t) + \tau^{\alpha}(E_{\mathrm{u}}{-}E_{\mathrm{r}})\mathrm{D}^{\alpha}\varepsilon(t). \tag{16}$$

is employed, where σ denotes the stress, E_{r} and E_{u} are relaxed and unrelaxed modulus, τ is the relaxation time, and D^{α} is the α order fractional derivative operator. The G1 numerical

Stiffness parameters (MPa)	Relaxation time (s)
$E_0 = 4.101$	
$E_1 = 0.378$	$\tau_1 = 1.60\times10^{-3}$
$E_2 = 0.427$	$\tau_2 = 2.91\times10^{2}$
$E_3 = 0.523$	$\tau_3 = 9.965$
$E_4 = 0.773$	$\tau_4 = 4.14\times10^{-1}$
$E_5 = 1.014$	$\tau_5 = 2.01\times10^{-2}$
$E_6 = 1.521$	$\tau_6 = 1.68\times10^{-3}$
$E_7 = 2.501$	$\tau_7 = 2.44\times10^{-4}$
$E_8 = 3.364$	$\tau_8 = 4.82\times10^{-5}$
$E_9 = 5.904$	$\tau_9 = 9.83\times10^{-6}$

Table 2. Coefficients for the Prony series fitted to the relaxation master curve.

approximation [43] of the fractional derivative of a generic function $f(t)$ at the instant $t_n$is used, given by

$$\mathrm{D}^{\alpha} f(t)|_{t=t_n} = \frac{1}{(\Delta t)^{\alpha}} \sum_{j=0}^{n-1} A_{j+1} f(t_{n-j}). \tag{17}$$

where $A_{j+1} = A_j(j-\alpha-1)/j$ with $A_1 = 1$, and Δt is the time step. Thus, applying a strain step as $\varepsilon(t) = \mathrm{H}(t)$ where $\mathrm{H}(t)$ is the Heaviside function, the relaxation modulus $E(t_n) = E_n$ where $t_n = n\times\Delta t$ can be calculated as

$$E_n = \frac{E_{\mathrm{r}} + (E_{\mathrm{u}}-E_{\mathrm{r}})\left(\frac{\tau}{\Delta t}\right)^{\alpha} \sum_{j=0}^{n-1} A_{j+1} - \left(\frac{\tau}{\Delta t}\right)^{\alpha} \sum_{j=1}^{n-1} A_{j+1} E_{n-j}}{1 + \left(\frac{\tau}{\Delta t}\right)^{\alpha}}. \tag{18}$$

An error minimization procedure has been applied for the curve fitting, and $E_{\mathrm{r}} = 3.271$ MPa, $E_{\mathrm{u}} = 20.147$ MPa, $\tau = 1.589\times10^{-7}$ s and $\alpha = 0.116$ have been determined.

In **Figure 18**, both models are compared with the experimental data.

From **Figure 18**, it should be noted that the fractional model has been fitted using a time step of $\Delta t = 1\times10^{-2}$ s. It should be pointed out that both models are able to reproduce the experimental relaxation master curve. Nevertheless, the curve provided by the fractional model is smoother. Besides, it should be pointed out that the fractional derivative model needs only four parameters whereas the generalized Maxwell model needs 19 parameters. On the contrary, the computation of Eq. (18) is much larger than that of Eq. (15). As a conclusion, it should be verified that relaxed and unrelaxed moduli provided by both models are coherent. Hence, it should be highlighted that involving the generalized Maxwell model, the unrelaxed modulus E_{u} can be calculated as

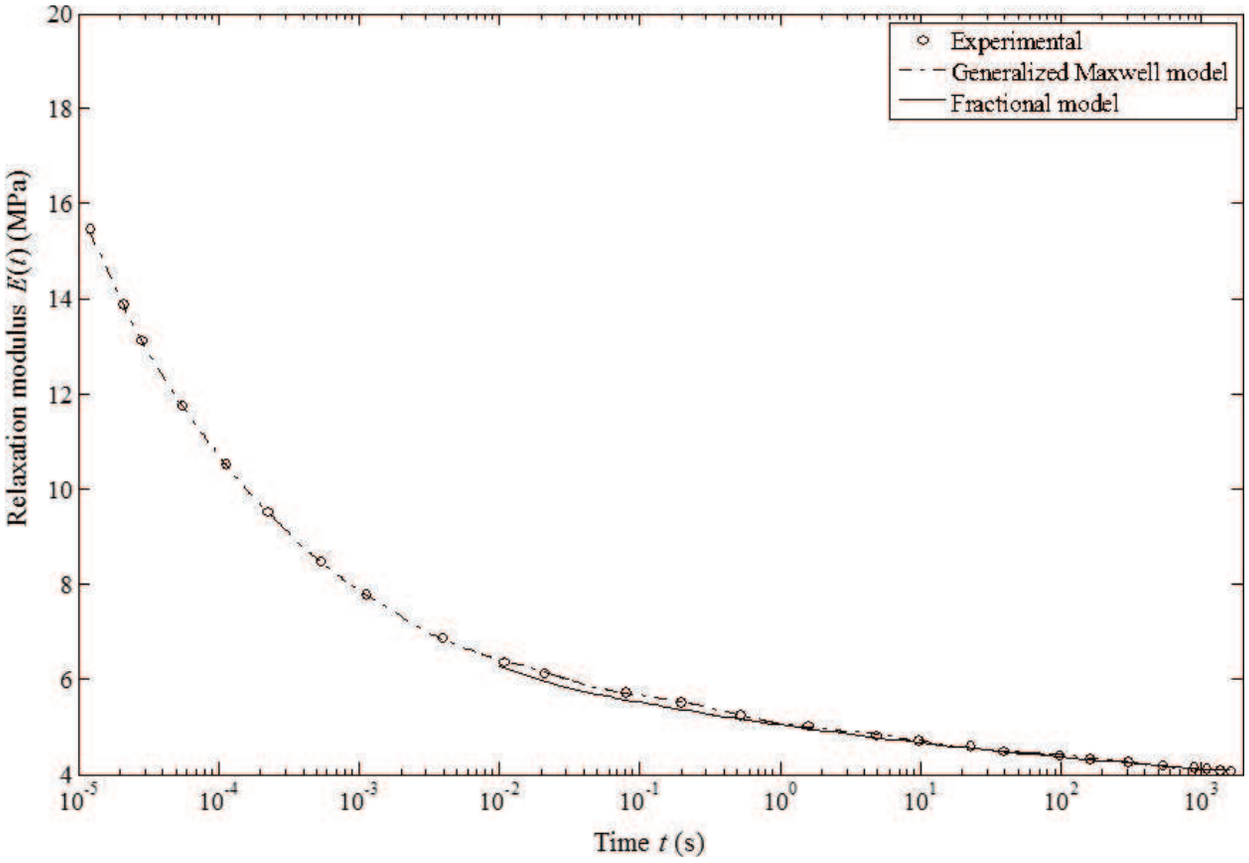

Figure 18. Relaxation models in time domain.

$$E_{\mathrm{u}} = E_0 + \sum_{i=1}^{N} E_i. \tag{19}$$

Hence, the obtained unrelaxed modulus E_{u} for the generalized Maxwell model is $E_{\mathrm{u}} = 20.806$ MPa while that for the fractional model is $E_{\mathrm{u}} = 20.147$ MPa.

Apart from the computational cost, fractional models describe precisely the viscoelastic behavior even in time domain despite the low number of parameters needed to describe wide time ranges [44–47].

2.3.2. Dynamic models

Following, the complex modulus $E^*(\omega)$ for the generalized Maxwell and fractional derivative models is derived from the Fourier transform of Eqs. (15) and (16), respectively. The one for the generalized Maxwell model yields

$$E^*(\omega) = E_0 + \mathrm{i}\omega \sum_{i=1}^{N} \frac{\tau_i E_i}{1 + \mathrm{i}\omega\tau_i}. \tag{20}$$

http://dx.doi.org/10.5772/66104

Stiffness parameters (MPa)	Relaxation time (s)
$E_0 = 5.049$	
$E_1 = 0.032$	$\tau_1 = 2.42\times10^{-7}$
$E_2 = 0.070$	$\tau_2 = 4.31\times10^{-3}$
$E_3 = 0.097$	$\tau_3 = 5.89\times10^{-3}$
$E_4 = 0.211$	$\tau_4 = 5.82\times10^{-3}$
$E_5 = 0.690$	$\tau_5 = 3.29\times10^{-1}$
$E_6 = 0.924$	$\tau_6 = 2.40\times10^{-2}$
$E_7 = 1.442$	$\tau_7 = 1.70\times10^{-3}$
$E_8 = 2.637$	$\tau_8 = 2.80\times10^{-4}$
$E_9 = 18.17$	$\tau_9 = 2.16\times10^{-5}$

Table 3. Coefficients for the Maxwell model fitted to the dynamic master curve.

where $\omega = 2\pi f$, f is the excitation frequency. The curve fitting is carried out by least squares with $N = 9$. The obtained numerical values are presented in **Table 3**.

Concerning the one based on fractional derivatives, the corresponding complex modulusresults in

$$E^*(\omega) = \frac{E_\mathrm{r} + (E_\mathrm{u} - E_\mathrm{r})(\mathrm{i}\omega\tau)^\alpha}{1 + (\mathrm{i}\omega\tau)^\alpha}. \tag{21}$$

Accordingly, fitting by least squares, $E_\mathrm{r} = 4.419$ MPa, $E_\mathrm{u} = 31.66$ MPa, $\tau = 1.17\times10^{-4}$ s and $\alpha = 0.353$ have been found, the regression coefficient satisfying $R^2 = 0.998$.

Both models, Eqs. (20) and (21), are contrasted to the experimental dynamic master curve shown in **Figure 19**.

From **Figure 19**, it should be highlighted that the generalized Maxwell model fits the experimental storage modulus $E^{'}$. However, the fractional derivative model reproduces better the experimental loss factor η. It should be remarked also that the fractional derivative model needs only four parameters. Besides, the fractional model parameters extraction Eq. (21) is faster than that of Eq. (20).

Involving the curve fitting, it should be noted that for time domain the difference between the unrelaxed modulus E_u provided by both models is 1.71%. Regarding frequency domain, the difference is 7.39%. However, for the relaxed modulus, the differences between the generalized and the fractional models for time and frequency domains are 20.24 and 12.47%, respectively. Consequently, the results provided by these models differs for $t \to \infty$ and for $f = 0$ Hz.

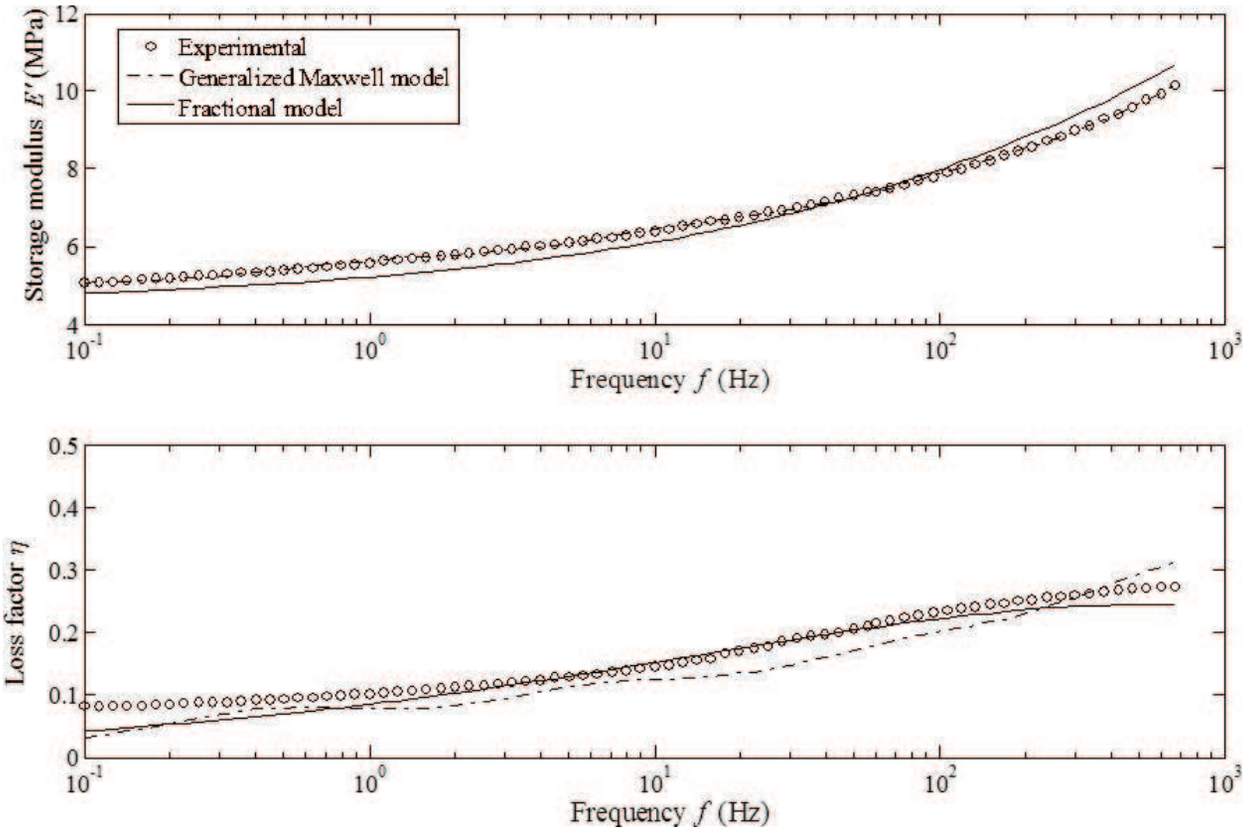

Figure 19. Dynamic models in frequency domain.

Hence, it can be stated that fractional derivative models are really valuable tools for describing the viscoelastic behavior principally in frequency domain but also in time domain [44–47].

2.4. Conclusions

The experimental characterization and modelization of the relaxation and complex moduli of the flexible adhesive ISR 70-03 havebeen performed using dynamic mechanical thermal analysis (DMTA).

- To conduct the experiments, defect-free samples have been manufactured using Teflon™ casts. Regarding validation, it can be concluded that tomography techniques by means of neutron radiography are able to identify internal and external defects in cured adhesives.
- Regarding the linearity, it can be stated that the relaxation test results are not influenced by sample thickness. On the contrary, the strain influence has been verified. Consequently, it has been modeled using an exponential model. Therefore, it can be noted that the material stiffens when the strain level decreases.
- Involving the master curves, the relaxation modulus $E(t)$ and the complex modulus $E^*(\omega)$ have been derived by means of a procedure based on the TTS principle. Besides, the temperature dependence has been modelized by the Arrhenius model.

- Finally, the generalized Maxwell model and fractional derivative models have been fitted to the time and frequency domains master curves. The generalized Maxwell one has been fitted using 19 parameters whereas the fractional derivative model has four parameters. Involving time domain, the fitting is accurate enough for both models. Regarding frequency domain, the storage modulus $E^{'}$ and loss factor η may be represented also by the generalized Maxwell and fractional derivative models. However, the fractional model fits the experimental response in a wide time or frequency ranges with a lower number of parameters. Hence, the fractional derivative model should be used for both time and frequency domains [44–47].

As a conclusion, a model capable of representing the influence of time, temperature and strain level over the mechanical properties of the flexible adhesive ISR 70-03 has been presented.

3. Relaxation modulus: complex modulus interconversion for linear viscoelastic adhesives

The interconversion path between the relaxation modulus $E(t)$ and the corresponding complex modulus $E^*(\omega)$ for linear viscoelastic solid materials is explored. The key difference with other approximate methods relies on the fact that in the presented procedure, the fast Fourier transform (FFT) algorithm is directly applied on the time-dependent part of the viscoelastic response $R(t)$. First, method foundations are outlined. Next, a theoretical example is developed using the generalized Maxwell model. Using this example, influence of sampling conditions and experimental error and data dispersion is studied. Finally, the accuracy of the method is proved by an application example using experimental data. As a conclusion, the proposed procedure is able to compute the complex modulus by means of relaxation tests and vice versa.

Concerning VEM behavior modeling, the memory of viscoelastic materials such as viscoelastic adhesives can be properly represented using the Boltzmann superposition principle [48]. Therefore, time evolution of stress $\sigma(t)$ can be evaluated using relaxation functions $R(t)$ through convolution integrals given by

$$\sigma(t) = E_{\mathrm{r}}\,\varepsilon(t) + \int_0^t R(t-\lambda)\dot{\varepsilon}(\lambda)\mathrm{d}\lambda. \tag{22}$$

where $\varepsilon(t)$ is the strain, E_{r} represents the viscoelastic constant, λ denotes the integration variable and $(.)$ represents the time derivative. In frequency domain, viscoelastic behavior can be represented by the complex modulus approximation [49], as shown in Eq. (4).

Concerning experimental characterization of viscoelastic adhesives, ASTM E 756-04 [10] details the methodology to characterize the mechanical behavior of non-self-supporting viscoelastic materials, implying the use of multimaterial Oberst beam specimens.

In this context, the DMTA technique allows to take into account together temperature and time (or temperature and frequency) by means of the time-temperature superposition (TTS) principle [24, 50] introducing no extra mass or damping.

Thus, frequency-time interconversion methods are valuable and useful tools [51–53] due to the fact that they can also be applied to overcome the inherent difficulties of relaxation or dynamic characterization [54–57], depending on the tested material. The most widely applied methods [51] for material functions conversion from time to frequency domains are those based on the Prony series model [40], and the opposed conversion can be achieved through the algorithms proposed by Ninomiya and Ferry [58]. The former can be obtained by fitting the experimental data by means of the generalized Maxwell model [59], whereas the latter is based on experimental data fitting.

As summary, the objective of this section is to propose an interconversion method between time and frequency domains capable of obtaining the complex modulus $E^*(\omega)$ by means of relaxation tests, and vice versa. The main advantage of this procedure is the direct application of the fast Fourier transform (FFT) algorithm on experimental data. On the contrary, other existing methods [55–65] are based on fitting models or theoretical functions. In particular, the proposed method is relevant when a Prony series cannot be accurately fitted to the experimental data in time or frequency domains. This section is structured as follows:

- Method foundations are outlined.
- A theoretical example is developed using a generalized Maxwell model. Using this example, influence of sampling conditions and experimental error and data dispersion are studied.
- The accuracy of the method is proved by an application example using experimental data.

3.1. Method foundation

An experimental relaxation test consists on applying a strain step as $\varepsilon(t) = \varepsilon_0 \mathrm{H}(t)$, where ε_0 represents the magnitude of the strain and $\mathrm{H}(t)$ is the Heaviside function. Consequently, applying a strain step and substituting its time derivative into Eq. (22), it yields

$$\sigma(t) = E_\mathrm{r}\, \varepsilon_0 \mathrm{H}(t) + \int_0^t R(t-\lambda)\, \varepsilon_0 \delta(\lambda) \mathrm{d}\lambda = [E_\mathrm{r} + R(t)]\varepsilon_0. \tag{23}$$

where $\delta(t)$ is the Dirac function. Then, the relaxation modulus $E(t)$ can be deduced as

$$E(t) = \frac{\sigma(t)}{\varepsilon_0} = E_\mathrm{r} + R(t). \tag{24}$$

where the long-term part of the relaxation modulus is represented by the viscoelastic constant E_r and where the time-dependent component is represented by $R(t)$.

Then, applying the Fourier transform, the complex modulus $E^*(\omega)$ is derived. On the one hand, applying the Fourier transform over Eq. (24), it results in

$$\tilde{E}(\omega) = \frac{E_r}{i\omega} + \tilde{R}(\omega) \tag{25}$$

where $(.)$ represents the Fourier transform. On the other hand, applying the Fourier transform over Eq. (1) it yields

$$\tilde{\sigma}(\omega) = E_r\, \tilde{\varepsilon}(\omega) + i\omega\, \tilde{R}(\omega)\, \tilde{\varepsilon}(\omega) \tag{26}$$

where from the complex modulus $E^*(\omega)$ can be derived, yielding

$$E^*(\omega) = E_r\ + i\omega\, \tilde{R}(\omega) \tag{27}$$

Therefore, by substituting the Fourier transform of the time-dependent part of the viscoelastic response $\tilde{R}(\omega)$ into Eq. (25), a relationship between complex modulus $E^*(\omega)$ and the Fourier transform of the relaxation modulus $\tilde{E}(\omega)$ is obtained,

$$E^*(\omega) = i\omega\, \tilde{E}(\omega) \tag{28}$$

As a result, the complex modulus $E^*(\omega)$ of a linear viscoelastic material can be obtained from the Fourier transform of its relaxation modulus $E(t)$. Nevertheless, applying the fast Fourier transform (FFT) algorithm, the resulting complex modulus $E^*(\omega)$ will suffer from leakage because $E(t)$ is not periodic [66, 67] and $E(t)_{t\to\infty} = E_r \neq 0$. Therefore, to avoid leakage, it should be remarked that the time-dependent part of the viscoelastic response $R(t)$ representing viscoelastic component disappears with time, $R(t)_{t\to\infty} = 0$. Hence, FFT algorithm does not produce leakage on complex modulus $E^*(\omega)$ approximation if Eq. (27) is used instead of Eq. (28). The drawback of the procedure is that the viscoelastic constant E_r must be extracted from the experimental data.

3.2. Theoretical example

Next, the influence of sampling conditions and experimental error and data dispersion is studied using an exponential material model. The study analyses some aspects related to the FFT algorithm, which are: leakage, signal discretization and the analyzed ranges. In this analysis, the FFT algorithm proposed by Cooley and Tukey [64] to compute the discrete Fourier transform is employed [65] despite the documented drawbacks [69]. There are other methods, as those presented by Dutt and Rokhlin [66] that have been used in several of applications [67–70]. However, as stated, the algorithm proposed by Cooley and Tukey [64] will be used.

An exponential damping model is widely used in the literature [71, 72], because it is capable of modeling damping mechanisms arising from viscoelastic nature of materials. Its time-dependent part of the viscoelastic response $R(t)$ is given by

$$R(t) = c\mu\, \mathrm{e}^{-\mu t} \tag{29}$$

resulting in a relaxation modulus as

$$E(t) = E_\mathrm{r} + E_1\, \mathrm{e}^{-\mu t} \tag{30}$$

where $\mu = \tau_\mathrm{m}^{-1} = E_1/c$ represents the material relaxation parameter, τ_m is the relaxation time, and E_1 and c are the stiffness and damping coefficients, respectively. The Fourier transform $\tilde{R}(\omega)$ of the time-dependent part of the viscoelastic response $R(t)$ is given by

$$\tilde{R}(\omega) = E_1 \frac{1}{\mu + \mathrm{i}\omega} \tag{31}$$

Accordingly, the complex modulus $E^*(\omega)$ yields

$$E^*(\omega) = E_\mathrm{r} + E_1 \frac{\mathrm{i}\omega}{\mu + \mathrm{i}\omega} \tag{32}$$

wherefrom storage modulus E' and loss factor $\tan\,\delta$ can be directly obtained as

$$E'(\omega) = E_\mathrm{r} + E_1 \frac{\omega^2}{\mu^2 + \omega^2} \tag{33}$$

and

$$\tan\delta(\omega) = \frac{E_1 \mu\omega}{E_\mathrm{r}\mu^2 + E_1(\mu^2 + \omega^2)} \tag{34}$$

respectively. For the numerical application, it is considered that $E_\mathrm{r} = 3$ MPa, $E_1 = 6$ MPa and $c = 0.1$ MPa s.

3.2.1. Leakage

Now, the leakage influence is studied. The conversion from time to frequency is achieved using the procedures described in Section 2 where the validation is done correlating the exact complex modulus (Eq. (32)) with that provided by Eqs. (28) and (27). All these complex modulus are represented in **Figure 20** as storage modulus E' and loss factor $\tan\,\delta$.

From **Figure 20**, it should be remarked that the direct use of Eq. (28) derives in erroneous results due to leakage, while through Eq. (27), the complex modulus $E^*(\omega)$ can be precisely computed from the relaxation modulus.

For the transformation from frequency to time domain, the exact relaxation modulus given by Eq. (30) is compared with those computed by the inverse FFT applied on Eqs. (28) and (27). Unfortunately, the leakage resulting from Eq. (28) provides a numerical instability, the relaxation modulus being infinity for every time. Thus, **Figure 21** illustrates only two curves instead of three: the analytic response given by Eq. (30) and the estimation for $E(t)$ by means of Eq. (27).

http://dx.doi.org/10.5772/66104

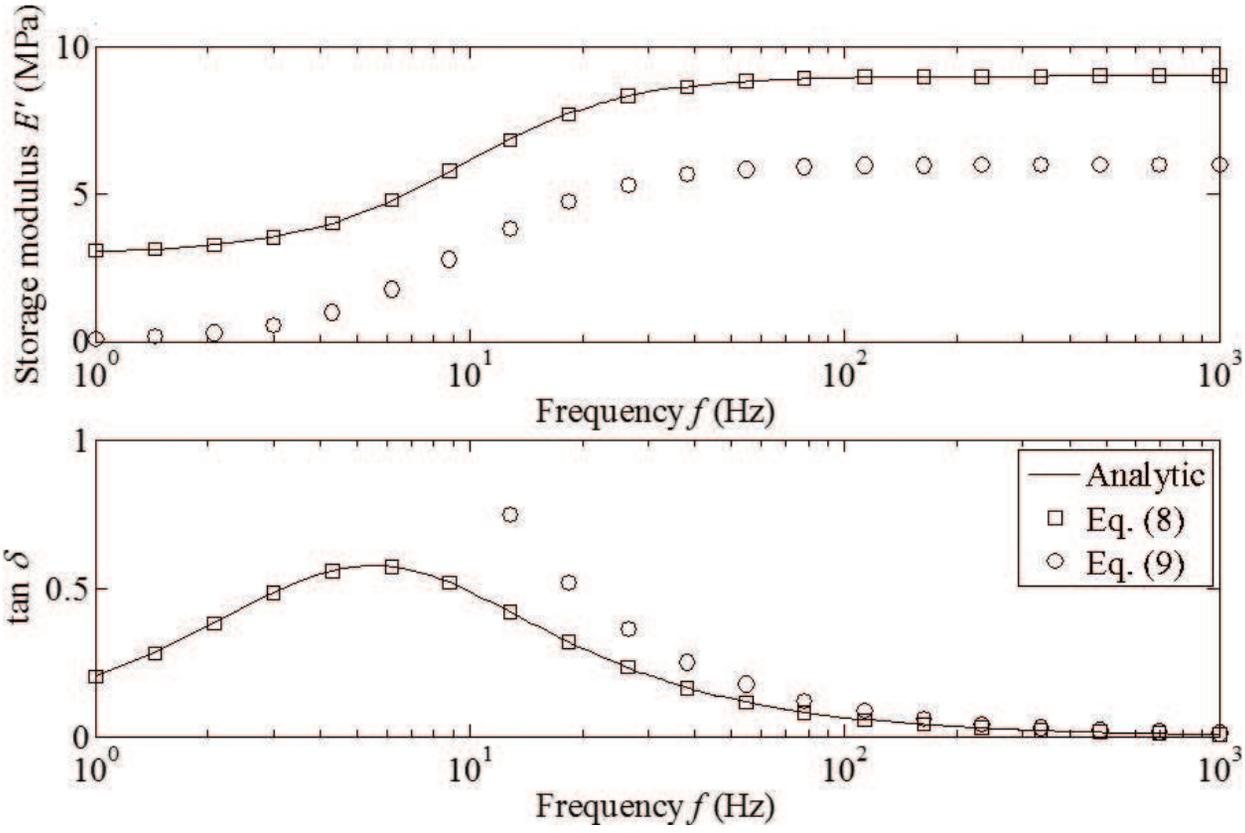

Figure 20. Influence of leakage, conversion from time to frequency. Comparison among the analytic generalized Maxwell model complex modulus $E^*(\omega)$ provided by Eq. (**32**), the one computed by means of Eq. (**28**) and therefore suffering leakage, and the one computed by means of Eq. (**27**) and therefore avoiding leakage.

From **Figure 21**, it should be pointed out that the proposed procedure is capable ofaccurately-computing the relaxation modulus $E(t)$ from the corresponding complex modulus $E^*(\omega)$.

3.2.2. Influence of time and frequency sampling

In this section, the influence of the time and frequency sampling is analyzed. It should be remarked that involving the conversion from time to frequency of a function defined up to a maximum time t_{max}, the discretization time Δt determines the Nyquist frequency f_{max}, according to

$$f_{max} = \frac{1}{2\Delta t} \tag{35}$$

the resulting discretized frequency being

$$\Delta f_{max} = \frac{1}{t_{max}} \tag{36}$$

having

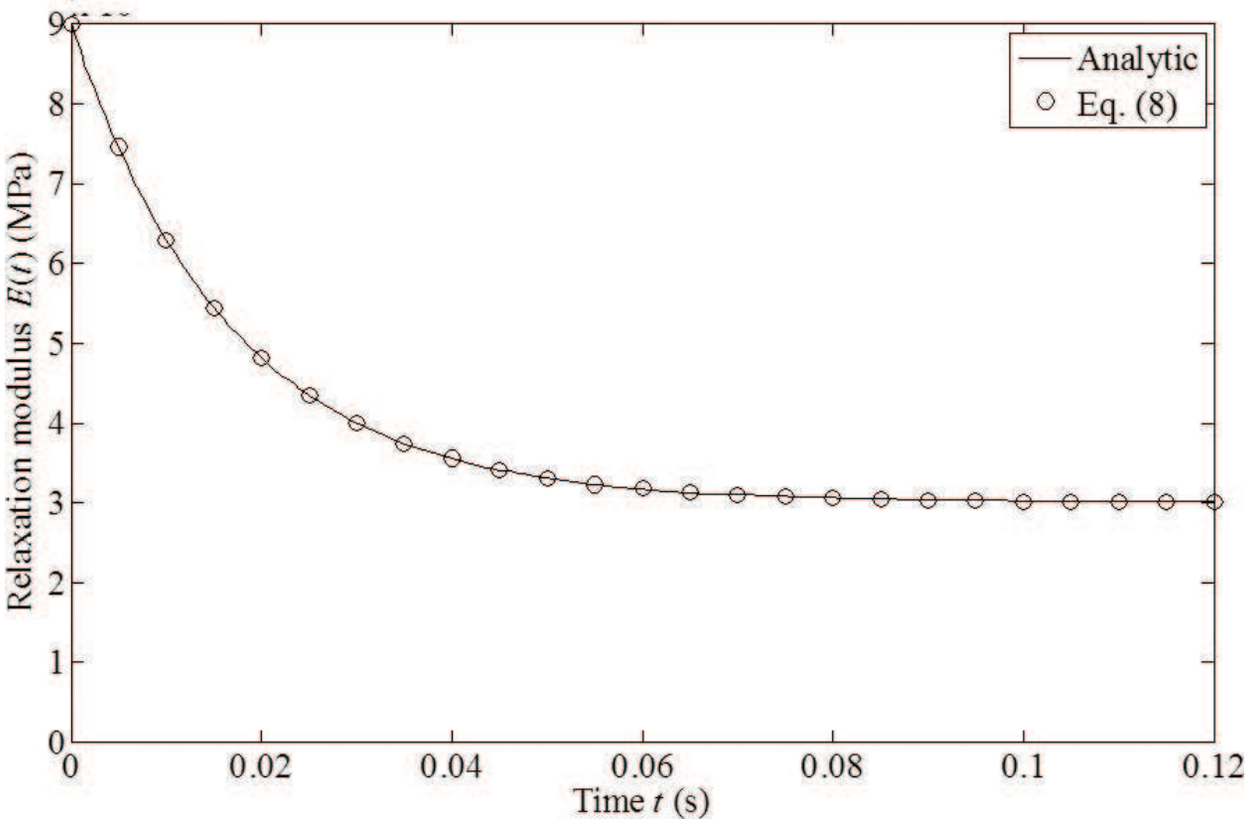

Figure 21. Influence of leakage, conversion from frequency to time. Comparison between the analytic generalized Maxwell model relaxation modulus $E(t)$ provided by Eq. (**30**), and the one computed through Eq. (**27**) avoiding leakage.

$$N = \frac{t_{\max}}{\Delta t} \tag{37}$$

discrete data.

For the conversion from frequency to time, these three equations can be inversely taken into account.

For the present analysis, $t_{\max} = 0.5$s is chosen, and five different discretization cases are analyzed: $\Delta t_1 = \tau_m/2 = 0.0083$ s, $\Delta t_2 = \tau_m/4 = 0.0042$ s, $\Delta t_3 = \tau_m/8 = 0.0021$ s, $\Delta t_4 = \tau_m/16 = 0.0010$ s and $\Delta t_5 = \tau_m/32 = 0.0005$ s. Thus, **Figure 22** shows six curves; the five analyzed cases plus the analytic response given by Eq. (30).

From **Figure 22**, it should be pointed out that the higher the Δt, the lower the $f_{\max}$ and better the accuracy. Thus, $\Delta t_1 = \tau_m/2$ is only able to represent the low-frequency range, representing the rubbery and the beginning of the transition zones of the viscoelastic material [54]. On the contrary, $\Delta t_5 = \tau_m/32$ is enough to accurately represent the complex modulus $E^*(\omega)$ in the whole frequency range, including the vitreous one [54].

For frequency to time domain transformation, a maximum frequency $f_{\max} = 1$ kHz is considered, and four discretization cases are studied: $\Delta f_1 = \tau_m^{-1}/2 = 29.94$ Hz, $\Delta f_2 = \tau_m^{-1}/4 = 14.97$ Hz,

http://dx.doi.org/10.5772/66104

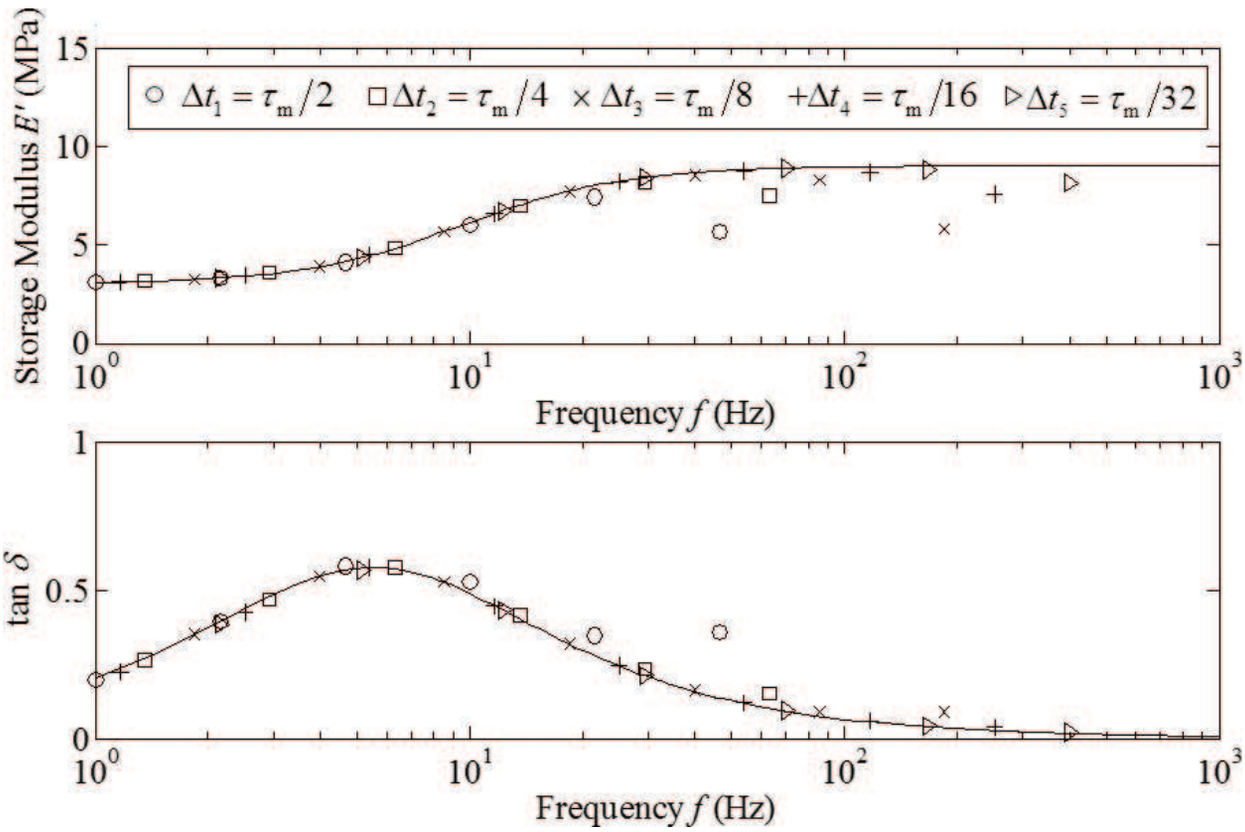

Figure 22. Influence of the analyzed time range, conversion from time to frequency. Comparison between generalized Maxwell model complex modulus $E^*(\omega)$ provided by Eq. (**32**) and the result provided by the proposed interconversion method for the different truncation times.

$\Delta f_3 = \tau_m^{-1}/8$ Hz = 7.48 Hz and $\Delta f_4 = \tau_m^{-1}/16$ Hz = 3.74 Hz. Hence, **Figure 4** shows five curves; the four analyzed cases and the analytic response given by Eq. (30).

From **Figure 23**, it should be noted that in two of the considered cases, $\Delta f_1 = \tau_m^{-1}/2$ and $\Delta f_2 = \tau_m^{-1}/4$, the relaxation is not properly represented. Thus, differences are verified for $t < 0.02$ s. Consequently, they are not useful to compute the relaxation modulus $E(t)$. Considering the cases $\Delta f_3 = \tau_m^{-1}/8$ and $\Delta f_4 = \tau_m^{-1}/16$, the relaxation is reached, providing analogous accuracy. Hence, for the present case, a $\Delta f_3 = \tau_m^{-1}/8$ is small enough to accurately compute the relaxation modulus $E(t)$.

3.2.3. Influence of the maximum time and frequency

Next, the influence of t_{max} and f_{max} is analyzed. First, the conversion from time to frequency is analyzed. The previously defined function discretization parameter Δt_5 is employed. Five truncated signals are considered, as $t_{max,1} = 2\tau_m = 0.0334$ s, $t_{max,2} = 4\tau_m = 0.0668$ s, $t_{max,3} = 8\tau_m = 0.1336$ s, $t_{max,4} = 16\tau_m = 0.2672$ s and $t_{max,5} = 32\tau_m = 0.5344$ s. On the one hand, **Figure 24** presents the exact $E(t)$ given by Eq. (30), in which each employed truncation is represented. On the other hand, **Figure 25** shows six curves corresponding to the five analyzed cases plus the analytic response given by Eq. (32).

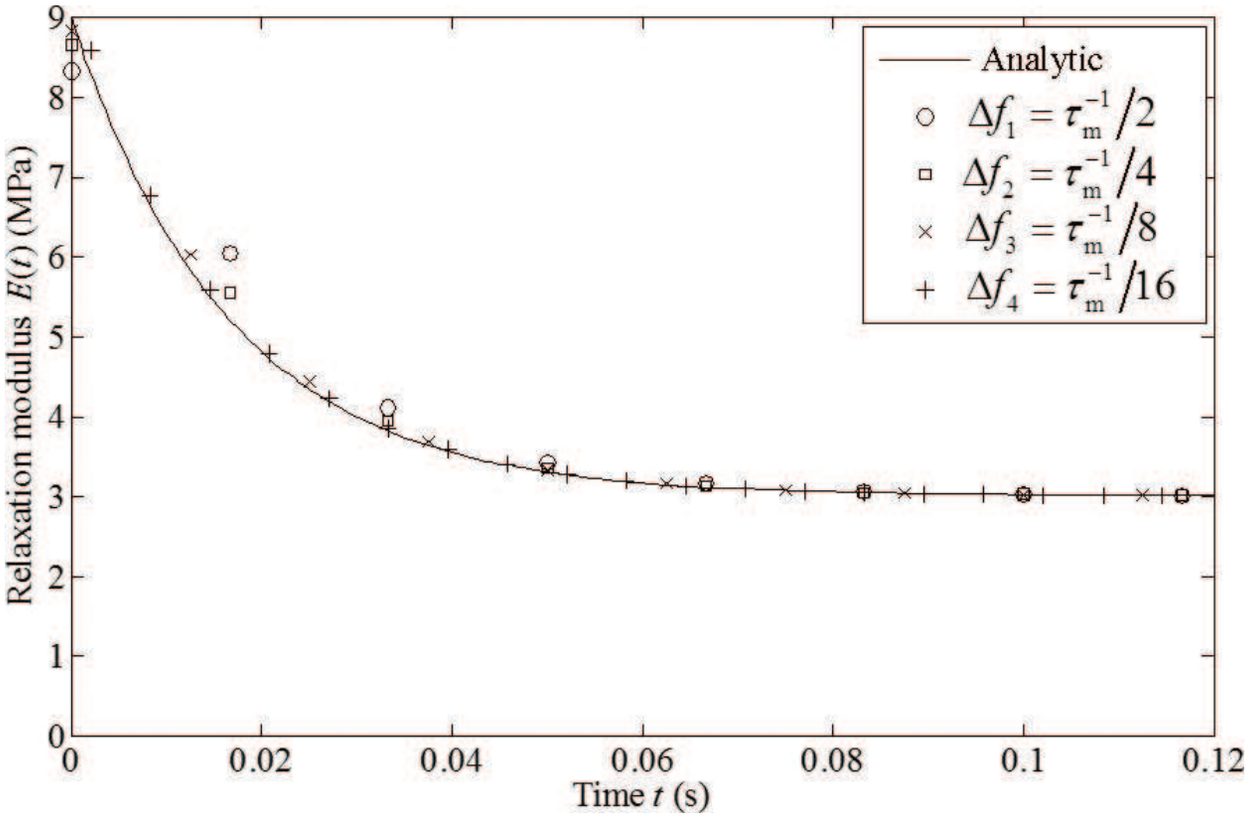

Figure 23. Influence of sampling frequency, conversion from frequency to time. Comparison between generalized Maxwell model relaxation modulus $E(t)$ provided by Eq. (**30**) and the result provided by the proposed interconversion method for different sampling frequencies.

From **Figure 24**, it should be remarked that in two of the considered cases, $t_{max,1}$ and $t_{max,2}$, the relaxation has not been reached, implying that only the vitreous zone can be represented, as **Figure 25** shows. Even if for $t_{max,3}$ and $t_{max,4}$ the relaxation has been reached, only the transition zone can be represented. In fact, to include the rubbery zone, a maximum spam $t_{max,5}$ has to be taken into account.

Next, for the conversion from the complex modulus to the relaxation modulus, a previously defined discretization frequency Δf_3 is chosen. Three cases of maximum frequency are analyzed: $f_{max,1} = 0.1\ \tau_m^{-1} \approx 6$ Hz, $f_{max,2} = \tau_m^{-1} \approx 60$ Hz and $f_{max,3} = 10\ \tau_m^{-1} \approx 600$ Hz. These frequency ranges are supposed to cover the rubbery, transition and vitreous zones, respectively, as shown in **Figure 26**. Therefore, **Figure 27** shows four curves matching to the three studied cases plus the analytic response given by Eq. (30).

From **Figure 27**, it should be noted that the lower the f_{max}, the worse the accuracy. Consequently, the $f_{max,1} = 0.1\ \tau_m^{-1} \approx 6$ Hz is not able to represent the relaxation modulus $E(t)$. Regarding $f_{max,2} = \tau_m^{-1} \approx 60$ Hz, differences are encountered during the relaxation until the viscoelastic constant E_r is reached. On the contrary, $f_{max,3} = 10\ \tau_m^{-1} \approx 600$ Hz is enough to accurately represent $E(t)$ in the whole time range.

http://dx.doi.org/10.5772/66104

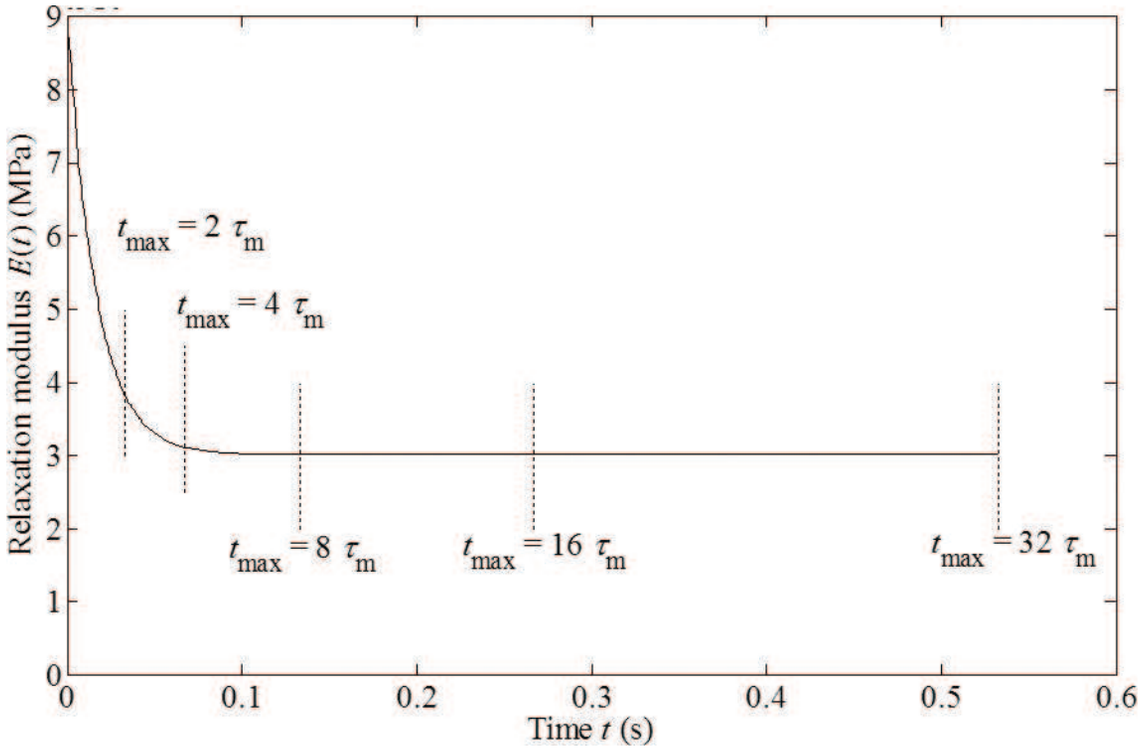

Figure 24. Influence of the analyzed time range, conversion from time to frequency. Analytic generalized Maxwell model relaxation modulus $E(t)$ provided by Eq. (**30**), in which different truncation times are illustrated.

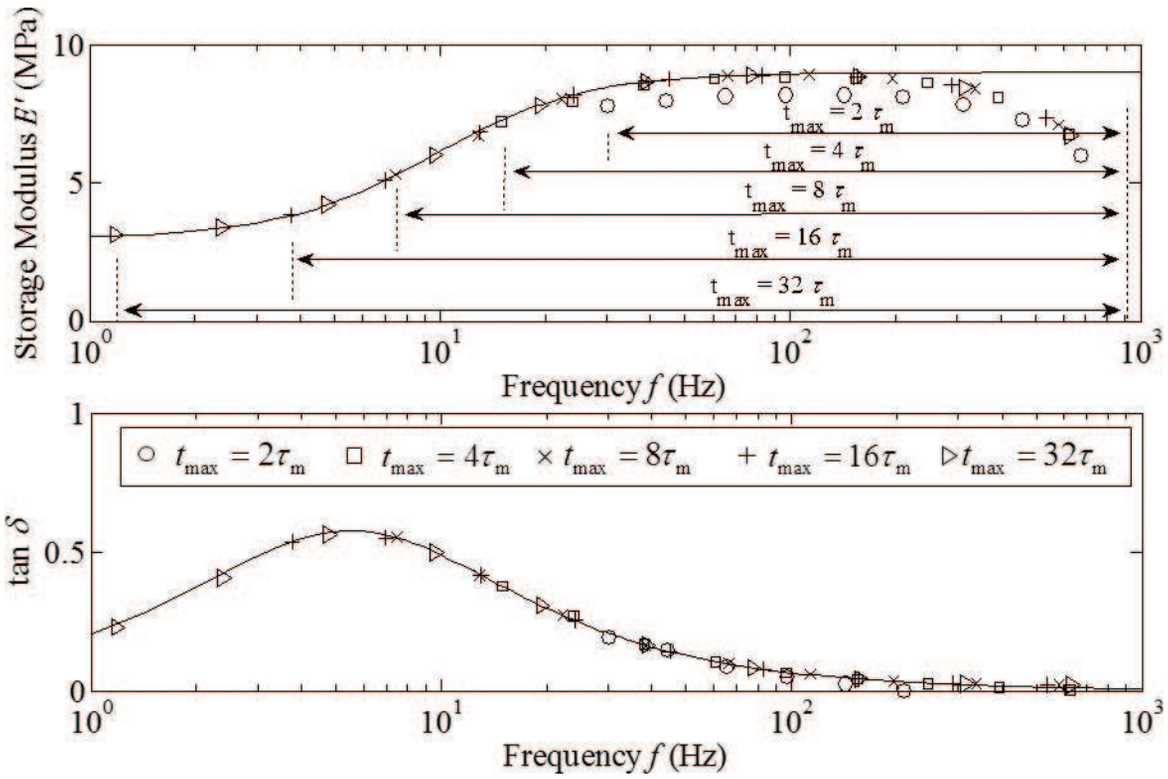

Figure 25. Influence of the analyzed time range, conversion from time to frequency. Comparison between the generalized Maxwell model complex modulus $E^*(\omega)$ provided by Eq. (**32**) and the result provided by the proposed interconversion method for the different truncation times.

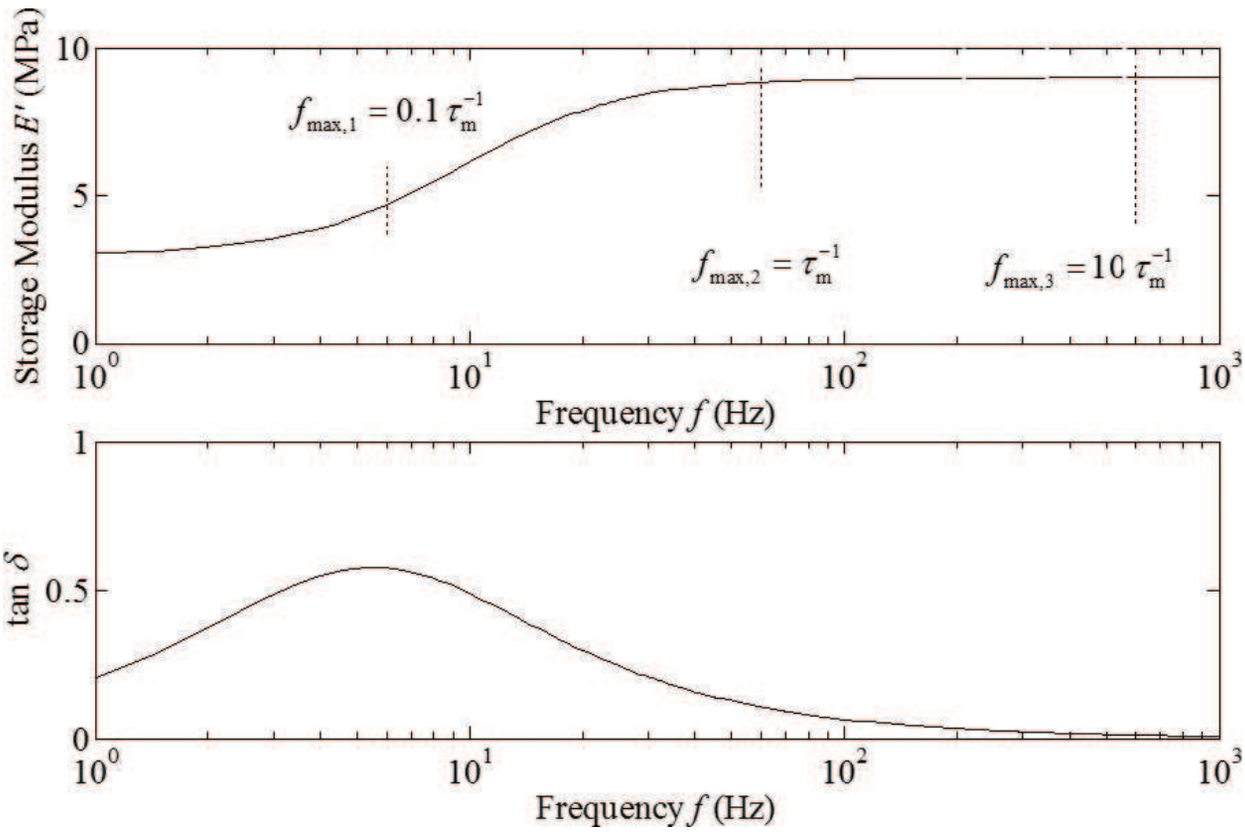

Figure 26. Influence of the analyzed frequency range, conversion from frequency to time. Analytic generalized Maxwell model complex modulus $E^*(\omega)$ provided by Eq. (**32**), in which different truncation frequencies are illustrated.

3.2.4. Influence of experimental error and data dispersion

Next, the precision of the interconversion is studied considering eventual data dispersion. Under this condition, some pseudo-experimental data for relaxation modulus$\overline{E}(t)$ and complex modulus $\overline{E}^*(\omega)$ have been generated evaluating Eqs. (30) and (32), respectively, in some unevenly spaced data points, in which random eventual error $\alpha(t)$ and $\alpha^*(\omega)$ have been introduced, as

$$\overline{E}(t) = E(t) + \alpha(t) \tag{38}$$

and

$$\overline{E}^*(\omega) = E^*(\omega) + \alpha^*(\omega) \tag{39}$$

Then, these generated data have been resampled in order to obtain evenly spaced data $\overline{E}_{es}(t)$ and $\overline{E}^*_{es}(\omega)$. For the present case, linear interpolation has been applied.

For the present numerical application, $\Delta t = 10^{-4}$s and $t_{max} = 1$ s are used. **Figures 28** and **29** show the conversion from relaxation modulus $E(t)$ to complex modulus $E^*(\omega)$. The former

http://dx.doi.org/10.5772/66104

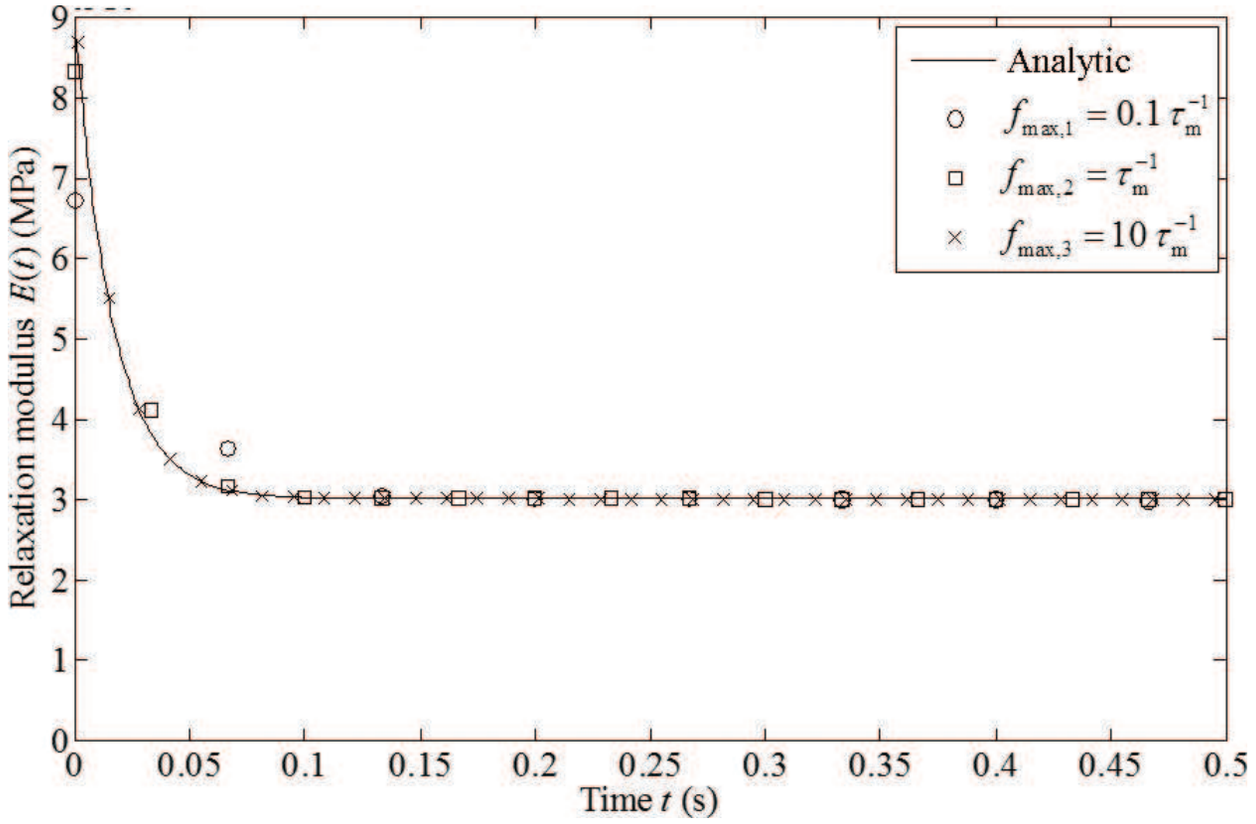

Figure 27. Influence of the analyzed frequency range, conversion from frequency to time. Comparison between the generalized Maxwell model relaxation modulus $E(t)$ provided by Eq. (**30**) and the result provided by the proposed interconversion method for different truncation frequencies.

illustrates Eq. (30) together with the pseudo-experimental data $\overline{E}(t)$ and the latter illustrates the converted modulus with the analytic solution for $E^*(\omega)$ given by Eq. (32).

From **Figure 29**, it should be pointed out that the low-frequency range is properly reproduced while the estimation of $E^*(\omega)$ for the higher frequencies differs from the analytic one (Eq. (32)). The reason is that not enough points were taken in $E(t)$ during the relaxation, and therefore, a linear interpolation technique is not enough to represent the employed model. Therefore, a higher number of data points are needed, especially during the relaxation. Besides, a higher order interpolation technique will provide better accuracy.

Regarding the inverse conversion, $\Delta f = 0.5$ Hz and $f_{max} = 1$ kHz are chosen to guarantee a wider time range. **Figures 30** and **31** show the conversion from complex modulus to relaxation modulus. **Figure 30** illustrates Eq. (32) with the pseudo-experimental data $\overline{E}^*(\omega)$, and **Figure 31** illustrates the converted modulus with the analytical solution for $E(t)$ given by Eq. (30).

From **Figure 31**, it should be noted that the converted relaxation modulus accurately reproduces the model provided by Eq. (30).

As a conclusion, it can be stated that the proposed procedure is able to provide an accurate approximation of the relaxation modulus $E(t)$ and of the complex modulus $E^*(\omega)$even though

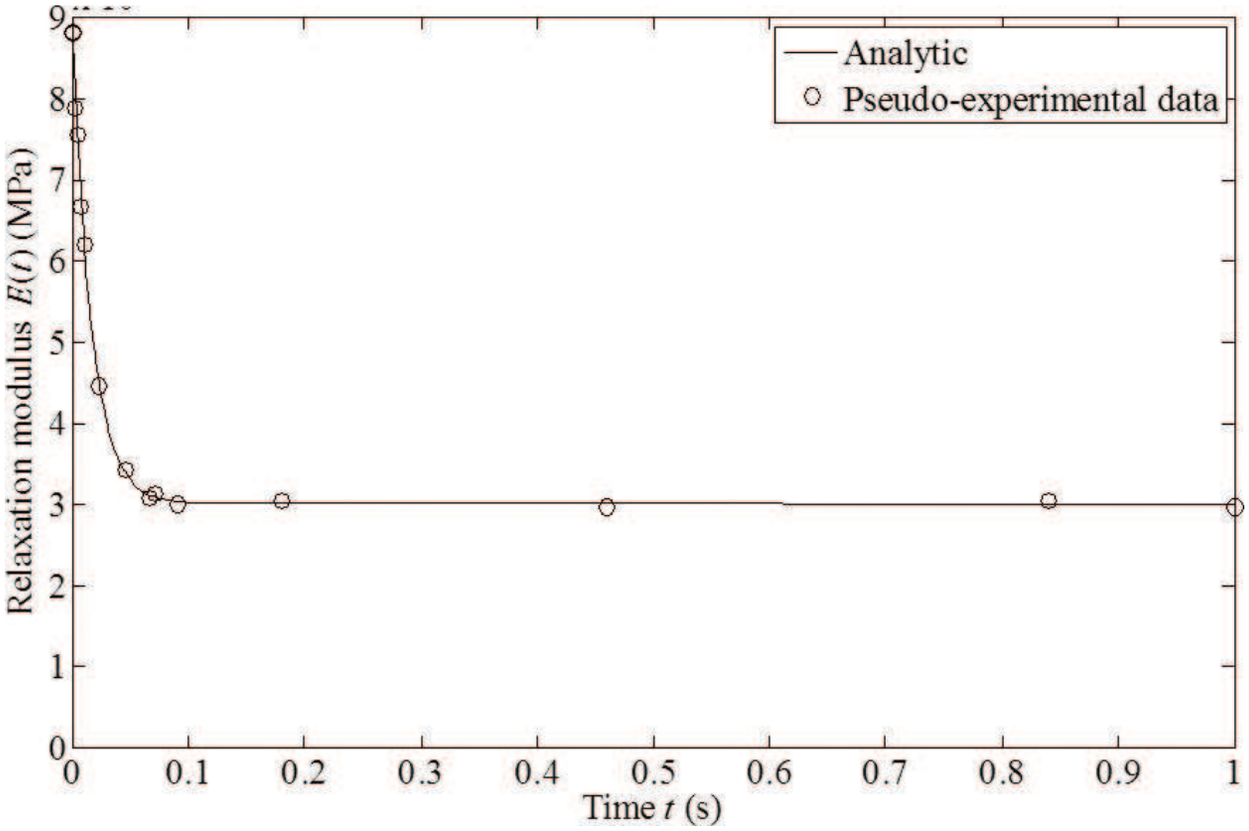

Figure 28. Influence of data dispersion, conversion from time to frequency. Analytic generalized Maxwell model relaxation modulus $E(t)$ provided by Eq. (**30**) together with the employed unevenly spaced data.

the original data does not match the exact response and even though data are not properly spaced.

3.3. Application example using experimental data

Finally, an application example is presented in which experimental data for DMTA obtained relaxation and complex moduli $E_{\text{exp}}(t)$ and $E^*_{\text{exp}}(\omega)$ of a flexible adhesive [73] are used to assess the present procedure. The employed flexible adhesive is a modified silane. Concretely, ISR 70-03 is employed [73]. It should be remarked that the behavior of the employed material was fitted to an exponential relaxation model [73] considering nine relaxation functions.

The experimental relaxation modulus $E_{\text{exp}}(t)$ covers the time range 10^{-5} s–3×10^{3} s while the complex modulus $E^*_{\text{exp}}(\omega)$ covers the frequency range 10^{-1} Hz–7×10^{2} Hz. It should be reminded that an interpolation technique is used to equally space the data. Also, this interpolation step is needed to reach the needed t_{max} and Δt where a cubic interpolation is employed. It should be remarked that, due to the fact that $E_{\text{exp}}(t)$ and $E^*_{\text{exp}}(\omega)$ are experimental data, there is no a relaxation time τ_{m} associated withthem as a result there is no underlying model. Thus, the desired Δt is estimated using the criteria $\tau_{\text{m}} = 0.66\, t_{\text{r}}$ where t_{r} is the elapsed time from the strain is applied until relaxation is reached. Therefore, a $\Delta t = 10^{-5}$ s is derived.

http://dx.doi.org/10.5772/66104

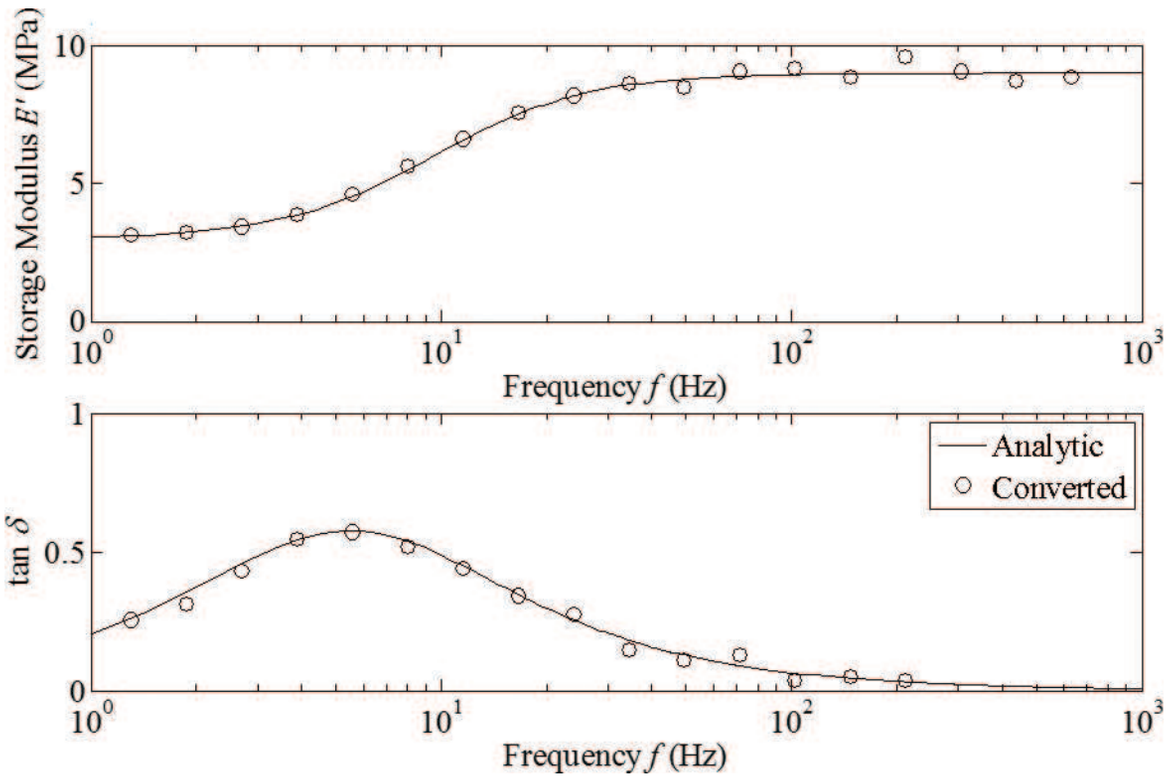

Figure 29. Influence of data dispersion, conversion from time to frequency. Comparison between analytic generalized Maxwell model complex modulus $E^*(\omega)$ provided by Eq. (**32**) and the converted one using data dispersion.

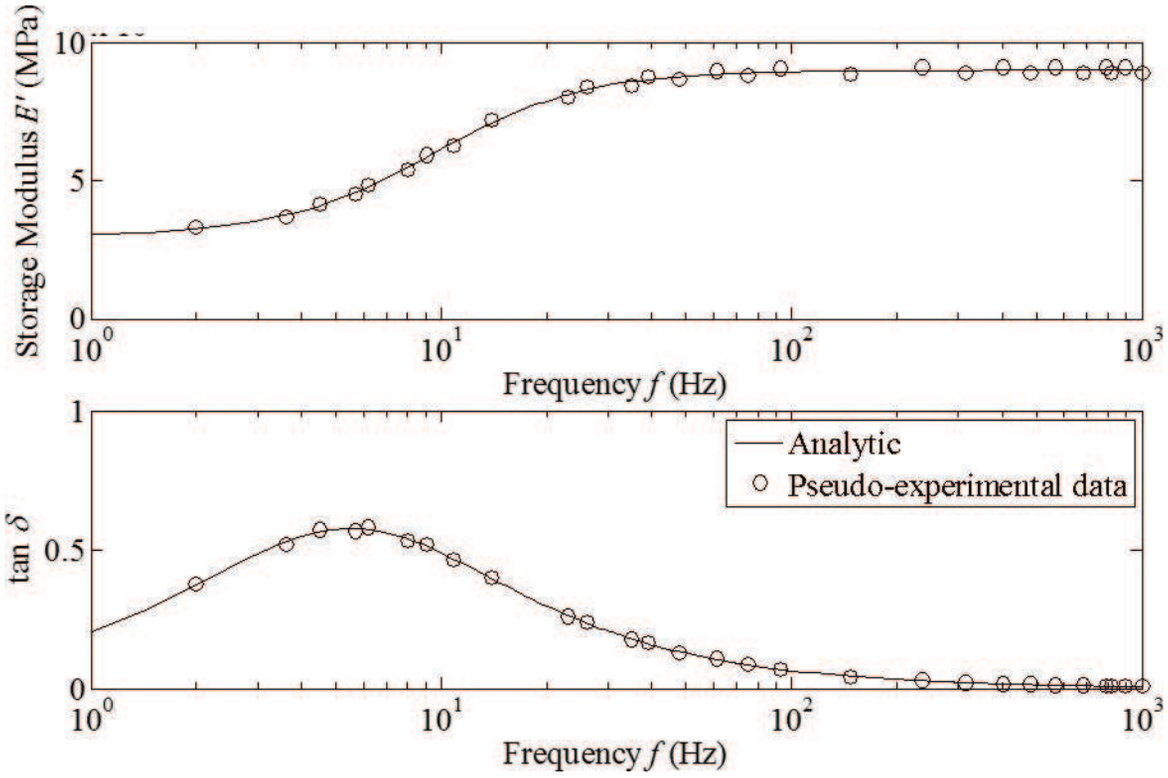

Figure 30. Influence of data dispersion, conversion from frequency to time. Analytic generalized Maxwell model complex modulus $E^*(\omega)$ provided by Eq. (**32**) together with the employed unevenly spaced data.

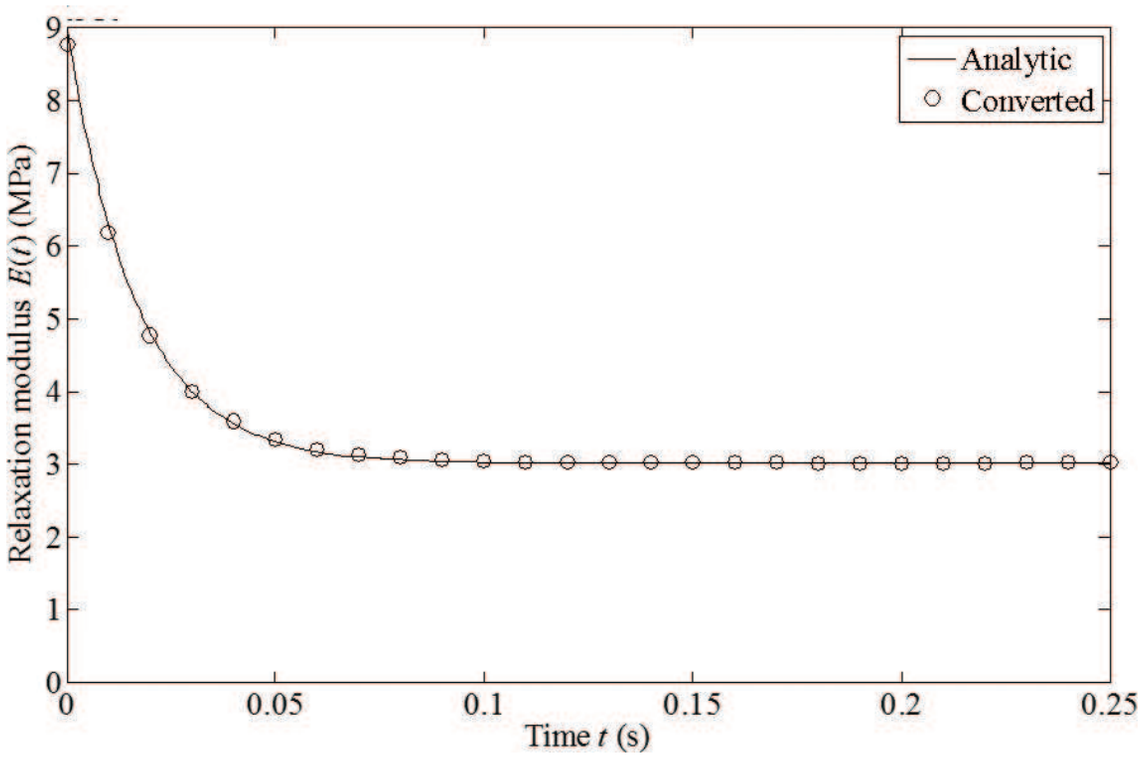

Figure 31. Influence of data dispersion, conversion from frequency to time. Comparison between analytic generalized Maxwell model relaxation modulus $E(t)$ provided by Eq. (**30**) and the converted one using data dispersion

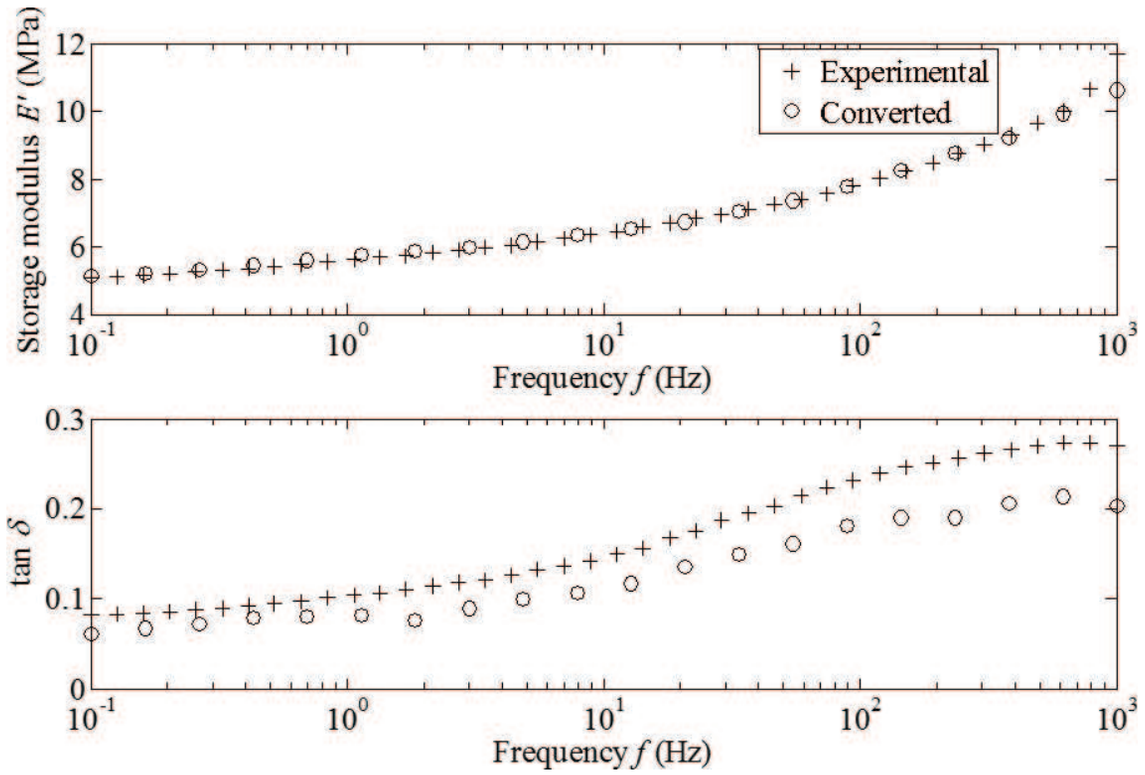

Figure 32. Application example using experimental results. Conversion from time to frequency: comparison between the experimental complex modulus $E^*(\omega)$ of a flexible adhesive and the converted one from its respective experimental relaxation modulus $E(t)$.

http://dx.doi.org/10.5772/66104

Regarding the dynamic case a $\Delta f = 0.01$ Hz is selected. Therefore, **Figure 32** shows the comparison of the conversion from relaxation modulus $E(t)$ to complex modulus $E^*(\omega)$ with the experimental data and **Figure 33** shows the inverse conversion.

From **Figure 32**, it should be pointed out that the described procedure achieves an accurate estimation for $E^*_{\text{exp}}(\omega)$. Regarding the storage modulus, the described procedure reproduces the experimental data in the whole frequency range. Concerning, the loss factor $\tan\delta(\omega)$, the procedure matches the tendency of the experimental data but differences are encountered, being significant in the high-frequency range where these grow up to 30%. Nevertheless, the accuracy of the interconversion can be improved by reducing the Δt used. Regarding the interconversion from frequency to time, from **Figure 33**, it should be noted that the described methodology provides a precise approximation for the experimentally obtained relaxation modulus during the relaxation. However, an error of 7% is found for the upper time limit. As it was presented in Section 3, the accuracy can be improved by reducing the Δf for the interpolation step or by widening the frequency range, this is employing a higher f_{max}.

3.4. Concluding remarks

In this section, the interconversion between the complex modulus $E^*(\omega)$ and the corresponding relaxation modulus $E(t)$for linear viscoelastic materials has been analyzed. In

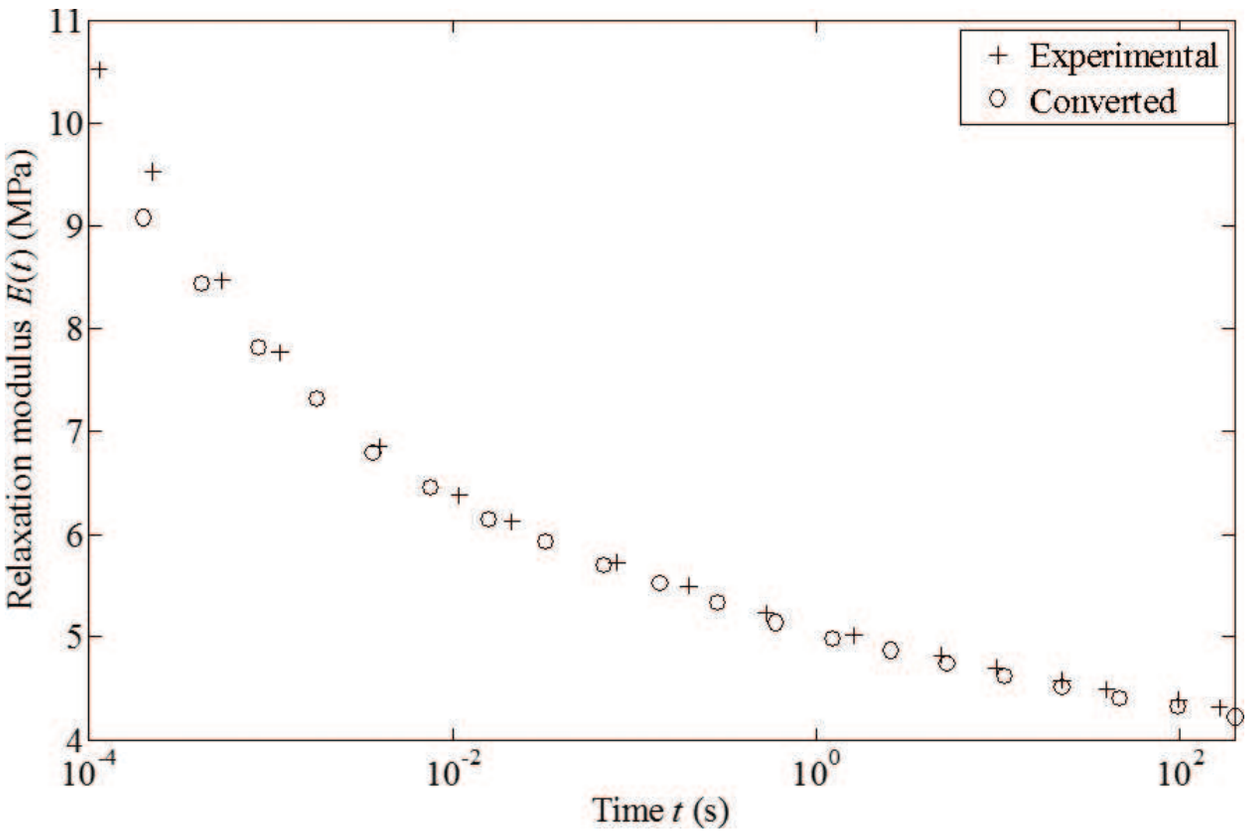

Figure 33. Application example using experimental results. Conversion from frequency to time: comparison between the experimental relaxation modulus $E(t)$ of a flexible adhesive and the converted one from its respective experimental complex modulus $E^*(\omega)$.

contrast to other approximate methods, in this research the FFT algorithm proposed by Cooley and Tukey has been applied on time-dependent part of the viscoelastic response $R(t)$. Together with the procedure itself, the influence of leakage, discretization and studied ranges so as the experimental error and data dispersion have been studied via an analytical material model. Also, an application case employing experimental data has been developed to prove the methodology. As a conclusion, the presented methodology is able to estimate the complex modulus $E^*(\omega)$ by means of relaxation tests, and vice versa.

4. Structural noise and vibration reduction in a cabin elevator prototype by means of adhesive-bonded joints of panels

This section presents an experimental study for the structural noise and vibration reduction in a cabin elevator by means of adhesive-bonded joints of panels. For that noise and vibration measurements are carried out on two prototypes: one of them built with classical panel joining technologies and the other one with adhesive joints. Through the experiments, the benefits from the vibroacoustic point of view of joining panels by means of adhesive-bonded joints in contrast to the traditional joining technologies are put into evidence.

4.1. Prototype description

Measurements are performed in order to prove adhesive joints benefits using the selected material. Therefore, in an elevator cabin property of ORONA S. Coop., the interior sound pressure level L_p was measured in conjunction with the vibration of a side panel $\ddot{s}(t)$. Besides, the vibrations of the floor of the cabin $\ddot{u}(t)$, $\ddot{v}(t)$, $\ddot{w}(t)$ in x, y and z directions, respectively, were also measured.

Hence, an elevator cabin prototype was built-up and two set of side panels were specifically manufactured. Thus, the results of the system with metallic joints are compared to those provided by the prototype system with adhesive joints. The experimental program was carried out under operational conditions and the analyzed frequency range is 5 Hz–1 kHz.

A scheme of both systems is shown in **Figures 34** and **35**, where **Figure 34** represents the position of the metallic joints, and **Figure 35** shows the system with the continuous adhesive single lap joints.

From **Figure 34**, it should be noted that two kinds of joints are employed in the original system. On the one hand, a joint typology is used between the basis and the side panel. On the other hand, another one is employed to join the metal sheets that constitute this side panel. From **Figure 35**, it should be pointed out that the adhesive joints are continuous; whereas the metallic ones are discrete joints. Besides, the joint thickness and overlapping length dimensions are $h_1 = 2$ mm and $l_1 = 50$ mm for the basis joint and $h_2 = 2$ mm and $l_2 = 20$ mm for the joint between the sheets.

Regarding the experiments, two kinds of responses were measured. On the one hand, the interior sound pressure level L_p was registered at the center of the cabin at a height of 1.5 m

http://dx.doi.org/10.5772/66104

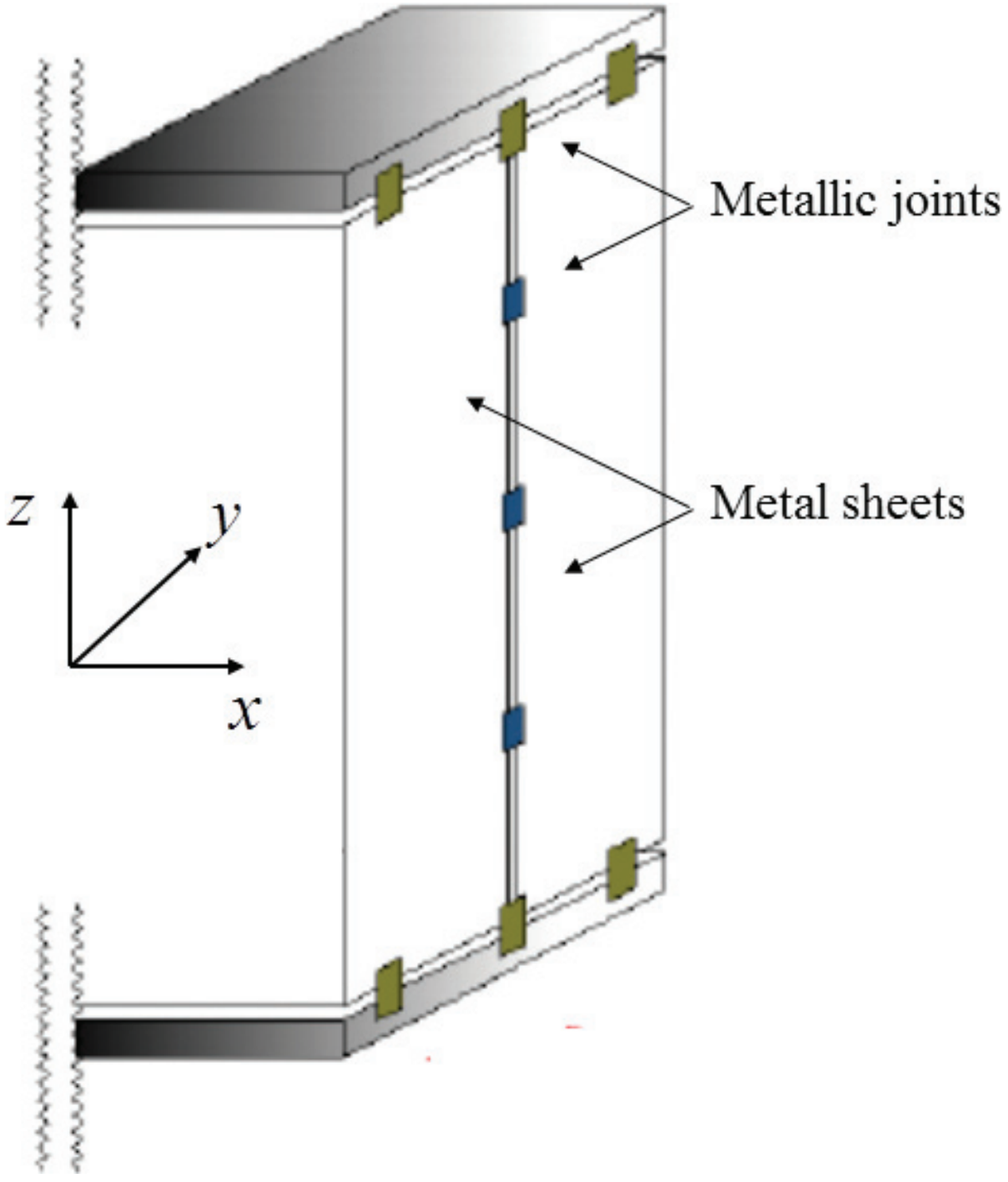

Figure 34. Original elevator scheme with metallic joints.

and facing to the side panel under study. On the other hand, the out of plane acceleration $\ddot{s}(t)$ of the side panel was measured. The floor accelerations $\ddot{u}(t)$, $\ddot{v}(t)$, $\ddot{w}(t)$ in x, y and z directions, respectively, were also registered.

Hence, **Figure 36** shows a scheme in which the placement of the accelerometers and the microphone is represented.

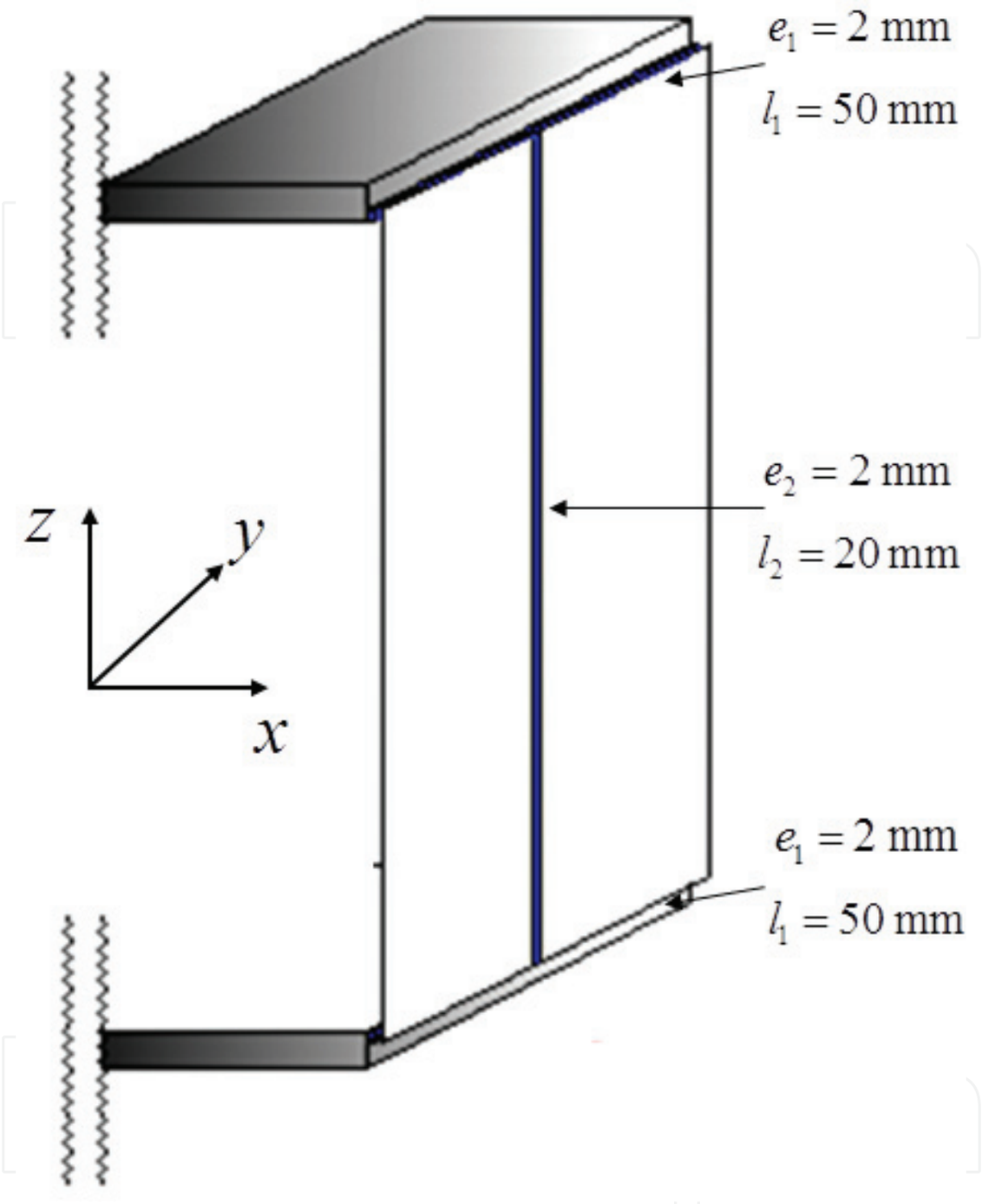

Figure 35. Prototype elevator scheme with adhesive joints.

Next, the responses of the elevator cabin with metallic joints are compared to those of the system with adhesive joints where the ISR 70-03 adhesive is employed. First, the sound pressure level L_p is analyzed together with the acceleration auto-spectrum of the side panel $\ddot{s}(t)$ (see **Figure 36**). Then, the floor acceleration auto-spectra in x, y and z directions are studied. The results are presented in third octave bands.

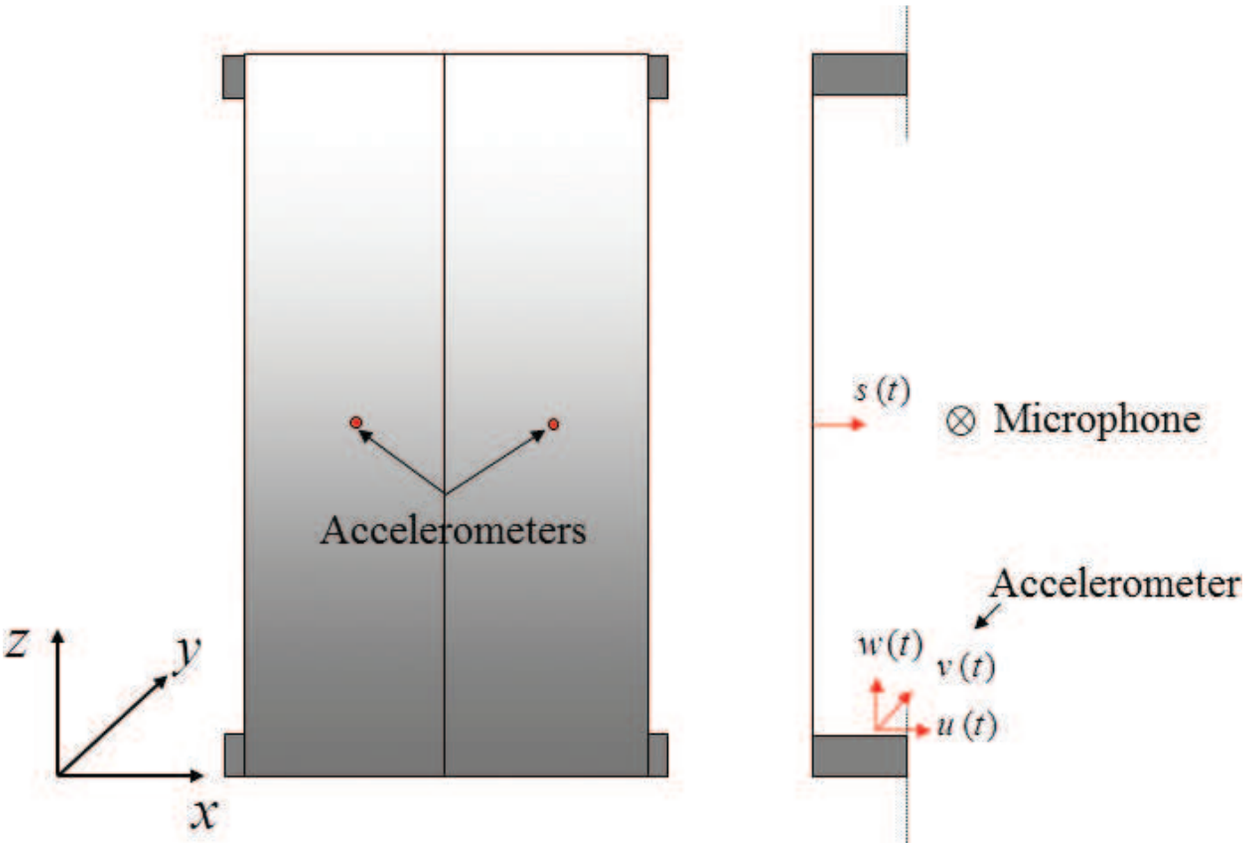

Figure 36. Representation of the elevator cabin measurement points.

4.2. Structural noise

Next, the sound pressure level inside the cabin is presented together with the vibration auto-spectrum of $\ddot{s}(t)$ for the right-hand side of the panel, that of the left-hand side one being analogous (see **Figure 36**). Hence, **Figure 37** shows the interior sound pressure level L_p for the system with metallic joints and the corresponding one for the system with adhesive joints. The results are presented using the A-weighting [74]. **Figure 38** shows both acceleration spectra of $\ddot{s}(t)$.

From **Figures 37** and **38**, it should be emphasized that the vibroacoustic response of an elevator cabin can be improved by adhesively bonding the side panels. Thus, according to **Figure 37**, the sound pressure level L_p has been reduced for even all frequency bands except for the one of 100 Hz. Small increments can be found also for the lowest frequency bands. Hence, the total sound pressure level has been determined, being $L_{p,\text{metal}} = 72.27$ dB for the system with metallic joints and $L_{p,\text{adh}} = 71.80$ dB for the one with adhesive joints. However, concerning the human ear, the A-weighting [74] is taken into account and the following values are reached: $L_{p,\text{metal}} = 50.89$ dB(A) and $L_{p,\text{adh}} = 49.59$ dB(A), respectively.

Hence, it can be concluded that the interior sound pressure level has been reduced by means of adhesive joints where a reduction of $\Delta L_p = 1.30$ dB(A) has been achieved. It should be

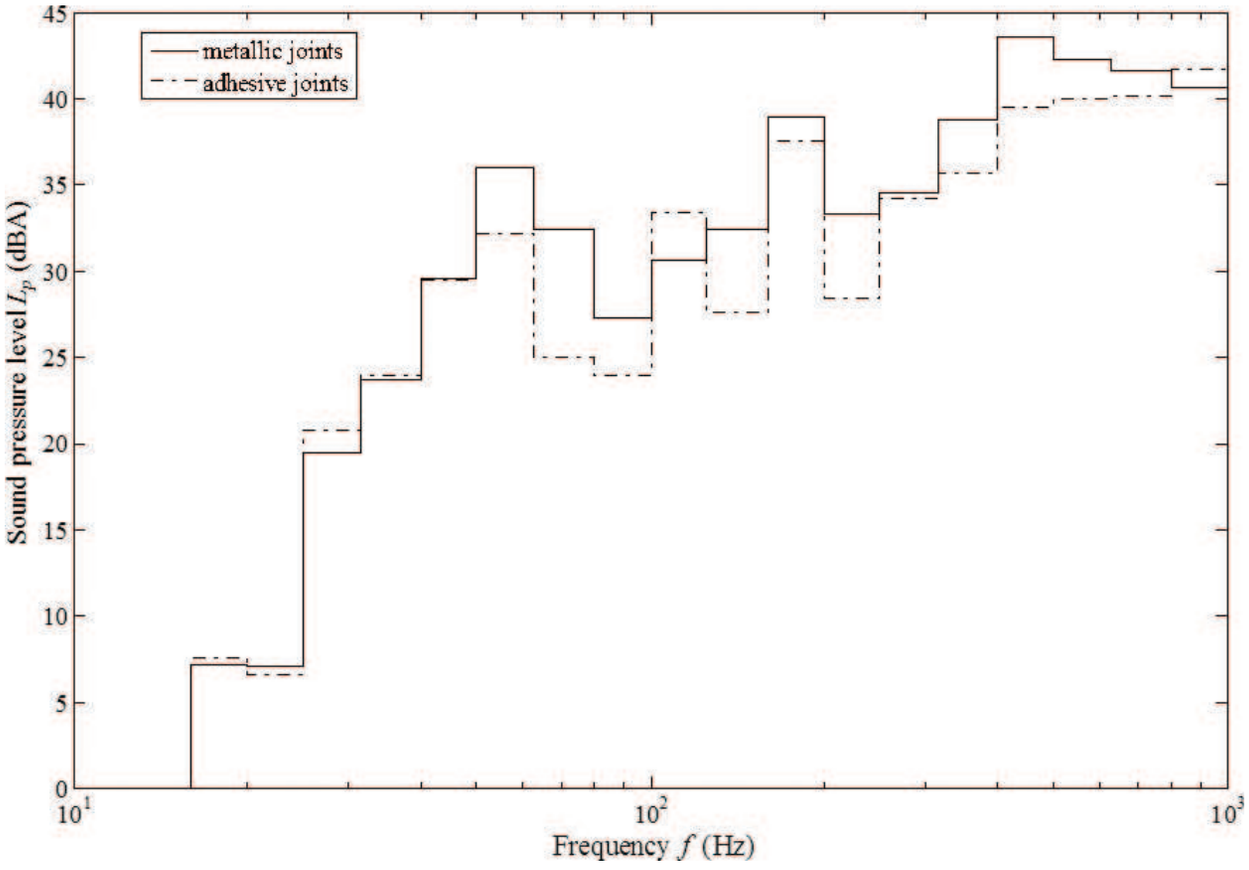

Figure 37. Structural noise response: sound pressure levels.

remarked that, for the present case only one of the three side panels has been adhesively bonded.

From **Figure 38**, it should be noted that the system with metallic joints contains the highest vibration levels in the low-frequency range, especially for frequencies smaller than 100 Hz. It is important to remark that these vibration levels are an order higher than those for higher frequencies.

In order to evaluate the effectiveness of the provided solution, the RMS acceleration $\ddot{s}_{RMS}$ has been computed, the result is shown in **Table 4**. The study is carried out taking into account two frequency groups: the first one made up by the frequency bands below 100 Hz and the second one by the frequency bands between 100 Hz and 1 kHz.

From **Table 4**, it should be pointed out that the level of vibration of the side panel has been reduced in 20 and 30% for the low and high frequency bands, respectively.

In short, it can be concluded that adhesive joints are able to reduce the interior structural noise of an elevator cabin, by means of introducing effective modal damping for the side panels.

http://dx.doi.org/10.5772/66104

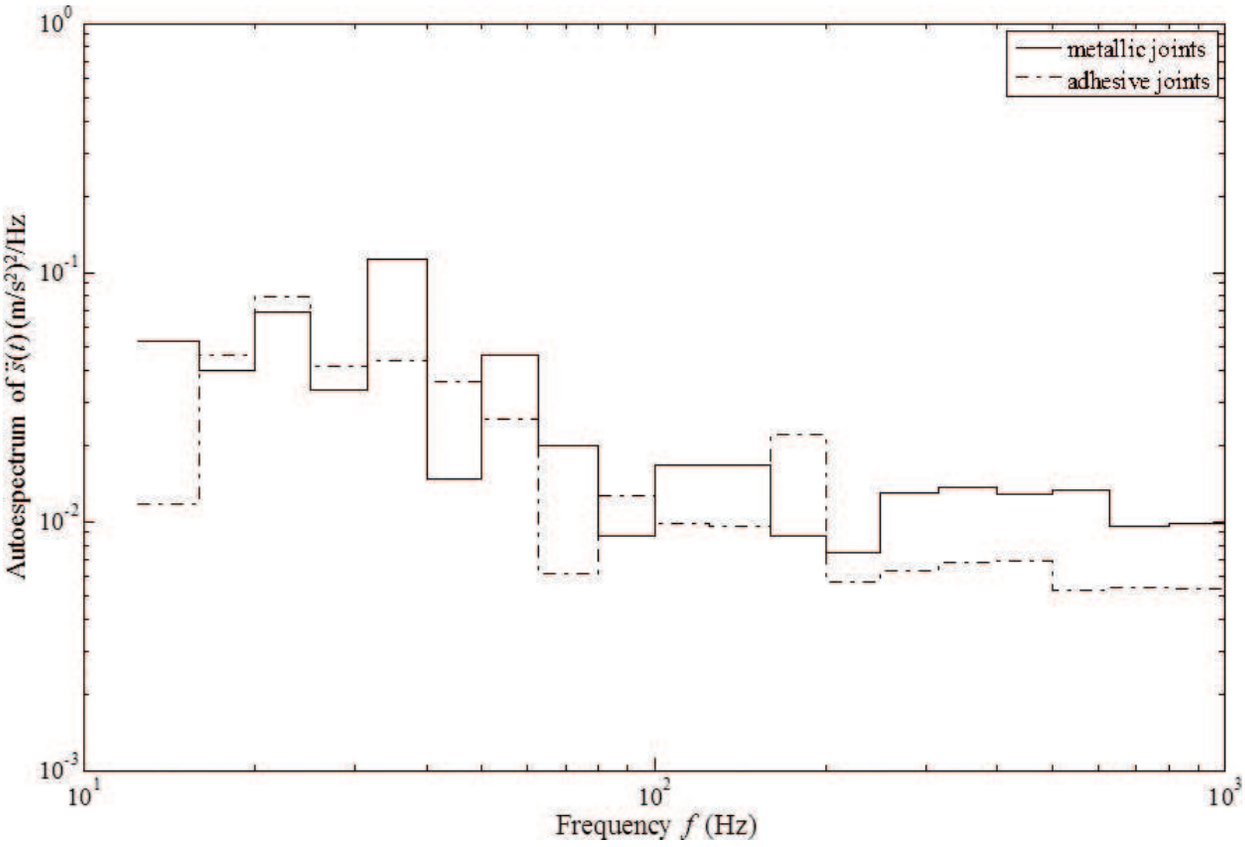

Figure 38. Structural noise response: auto-spectrum of $\ddot{s}(t)$.

		$\ddot{s}_{\text{RMS}}$ $(\text{m/s}^2)^2$	$\ddot{u}_{\text{RMS}}$ $(\text{m/s}^2)^2$	$\ddot{v}_{\text{RMS}}$ $(\text{m/s}^2)^2$	$\ddot{w}_{\text{RMS}}$ $(\text{m/s}^2)^2$
$f < 100$ Hz	Metallic	1.82	1.06	0.83	2.03
	Adhesive	1.48	0.86	0.76	1.72
100 Hz $< f <$ 1 kHz	Metallic	3.64	3.23	3.02	3.50
	Adhesive	2.53	2.00	1.89	2.44

Table 4. Vibrational results.

4.3. Vibration floor response

Next, the vibration spectra of the cabin floor are presented. The aim of this analysis is to verify that the vibrational ride comfort has not been decreased by the use of adhesive joints. **Figures 39–41** illustrate the acceleration auto-spectra for $\ddot{u}(t)$, $\ddot{v}(t)$ and $\ddot{w}(t)$, respectively, for the systems with metallic and adhesive joints.

From **Figures 39–41** it should be pointed out that, accordingly to the panel response, the highest vibration levels are found for frequencies below 100 Hz. Concerning **Figures 40** and **41**, it should be noted that the smallest vibration level is encountered for the medium-frequency

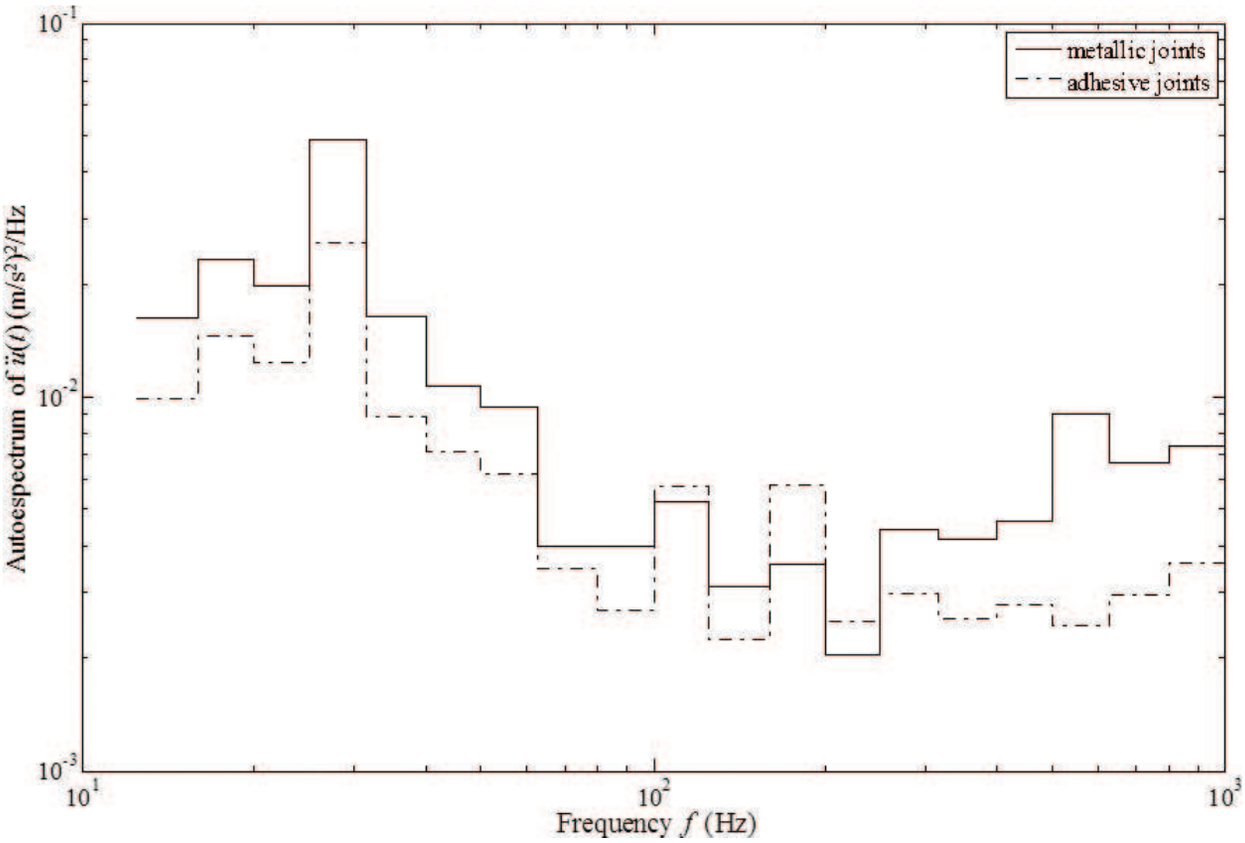

Figure 39. Cabin floor response acceleration auto-spectra in the x direction.

range. It is worth mentioning that the acceleration level on the z direction, see **Figure 41**, is one order of magnitude higher than those for x and y directions. The obtained RMS acceleration values for the systems with metallic and adhesive joints are shown in **Table 4**. The results are provided in two frequency bands as well.

From **Table 4**, it should be pointed out that in spite of just one side panel has been joined with the adhesive material its effect over the vibrational response of the floor is significant. Thus, for the horizontal vibration a reduction up to 40% is obtained while the vertical vibration level has been reduced to 30%.

4.4. Conclusions

In this section, a study for the noise and vibration reduction in an elevator cabin prototype by means of panel adhesive-bonded joints has been presented. The interior sound pressure level of the considered elevator cabin prototype has been reduced in $\Delta L_p = 1.30$ dB(A). The vibration level of the side panel has been significantly reduced in the low and high frequency bands. Also, the vibration level of the elevator cabin floor has been reduced also.

As conclusion, taking into account the presented results obtained with adhesive joints in only side panels, ride comfort in an elevator cabin can be notably enhanced by substituting traditional joining technologies by adhesive-bonded joints.

http://dx.doi.org/10.5772/66104

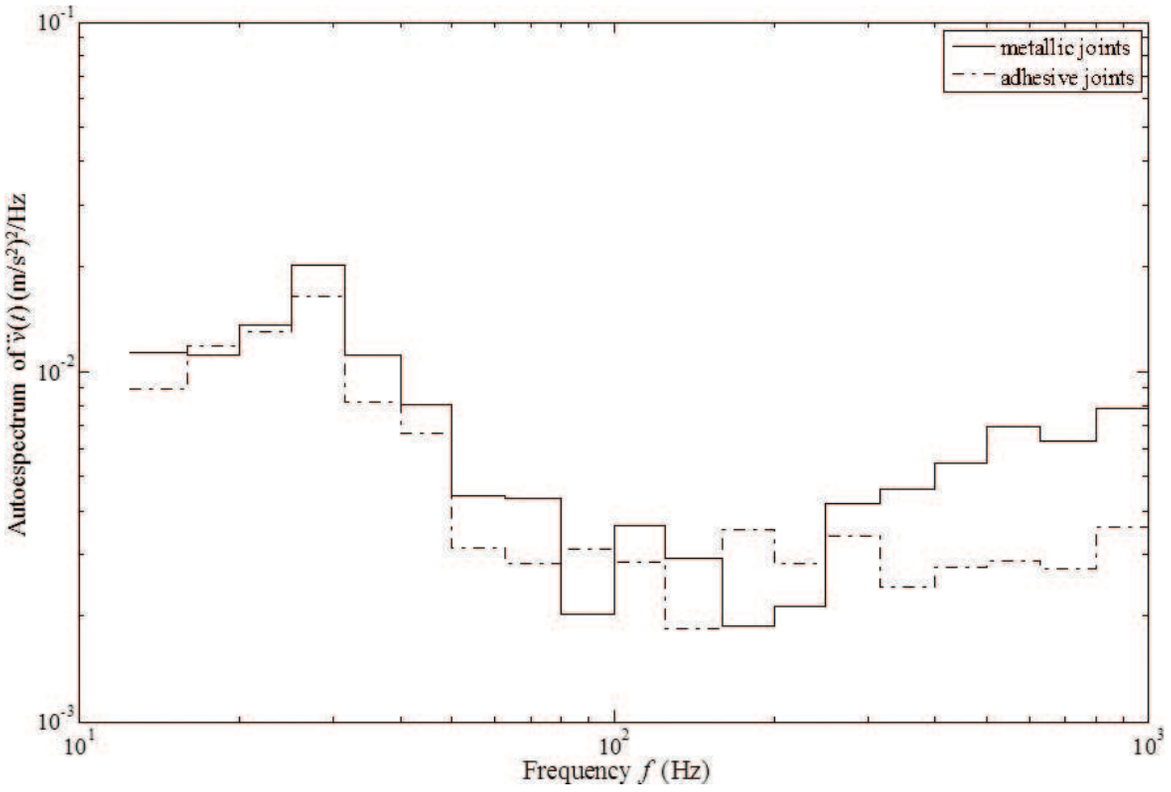

Figure 40. Cabin floor response acceleration auto-spectra in the y direction.

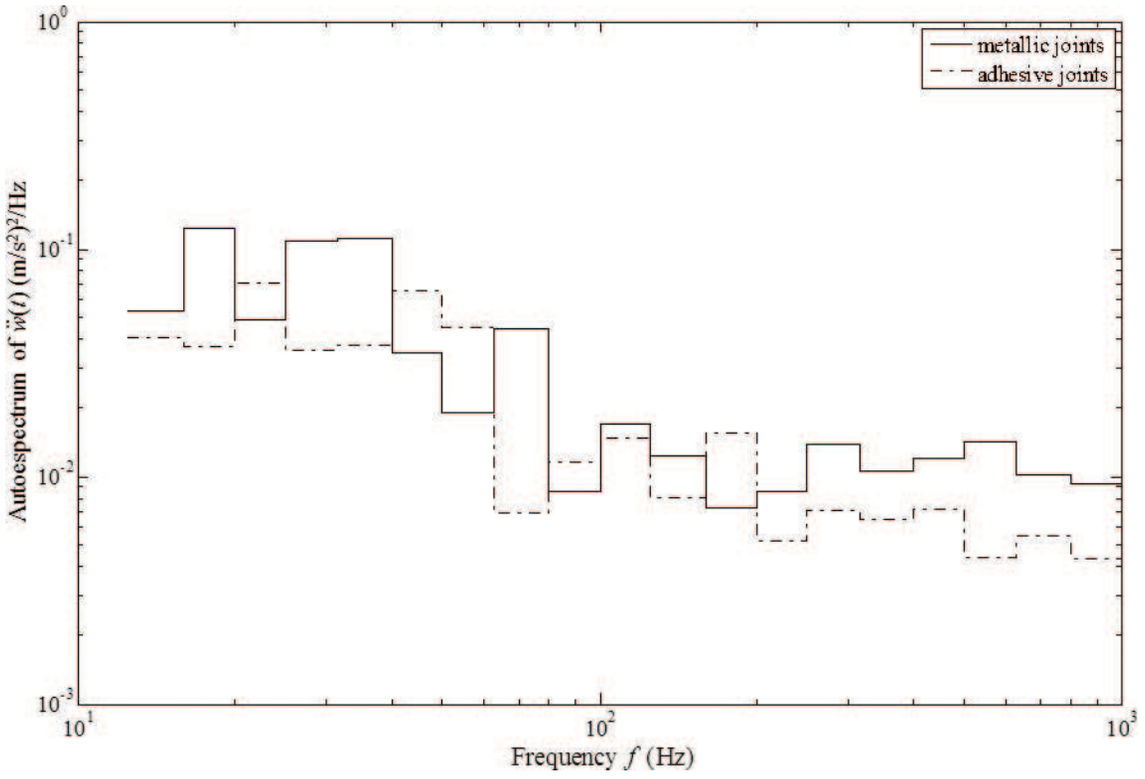

Figure 41. Cabin floor response acceleration auto-spectra in the z direction.

5. Chapter conclusions

This chapter has been focused on the dynamic characterization of adhesive materials for vibration control proposes. First, the experimental characterization and modelization of the relaxation and complex moduli of the flexible adhesive ISR 70-03 by means of a dynamic mechanical thermal analysis technique (DMTA) has been presented. Then, the interconversion path between the relaxation modulus $E(t)$ and the corresponding complex modulus $E^*(\omega)$ for linear viscoelastic solid materials has been explored. In contrast to other approximate methods, in this work the fast Fourier transform (FFT) algorithm has been directly applied on relaxation functions. Finally, an experimental study for the structural noise and vibration reduction in a cabin elevator by means of adhesive-bonded joints of panels has been presented to probe the benefits of adhesive joints on the vibroacoustic behavior of equipment subjected to dynamics loads.

Acknowledgements

Parts of this chapter are reproduced from authors' recent work [73, 75].

Author details

Jon García-Barruetabeña* and Fernando Cortés Martínez

*Address all correspondence to: jgarcia.barruetabena@deusto.es

Faculty of Engineering, University of Deusto, Bilbao, Spain

References

[1] Feng L. An experimental method to determine vibroacoustic properties of joints. In: Euro Noise International INCE Symposium; Washington, DC INCE/USA 1998. pp. 1–6.

[2] Feng L. Characterization methods and ranging of mechanical joints. In: ISMA05; San Antonio, Texas 2000. pp. 793–800.

[3] Feng L. An experimental method for vibration insertion loss of mechanical joints. ACUSTICA. 2001;**87**:191–198.

[4] Feng L., Liu M. Experimental study of structure-borne sound transmission loss of mechanical joints. Acoustical Society of America. 2001;**110**(3):1391–1397.

[5] Feng L. Vibration reduction through joint in finite systems. In: Proceedings InterNoise; Christchurch, New Zealand 1998. pp. 655–670.

[6] Zatarain M., Villasantea C. New light and highly-damped bonded structures for noise and vibration reduction. Cirp Annals. 2007;**53**(1):345–348.

[7] Bostik industry. Bostik Industry, Technical Sheet for Industrial Special Range (ISR) 70–03. English version [Internet]. Available from: http://www.bostikindustrie.nl [Accessed: 15 December 2010]

[8] Watrnaka G.M. Strain-frequency temperature relationships in polymers. Journal of Engineering for Industry. 1968;**90**(3):491–498.

[9] Sjöberg M. On Dynamic Properties of Rubber Isolators. [thesis]. KTH: 2002.

[10] ASTM E 756–04. Standard test method for measuring vibration damping properties of materials. American Society for Testing and Materials. 2004.

[11] Fasana A.G. Oberst beam test technique. Proceedings of the Society of Photo-Optical Instruments. 1998;**3327**:451–462.

[12] Wojtowickia J.L., LucJ. New approach for the measurement of damping properties of materials using the Oberst beam. Review of Scientific Instruments. 2004;75(8) 2569–2581.

[13] Caracciolo R.,Gasparetto A., Giovagnoni M. An experimental technique for complete dynamic characterization of a viscoelastic material. Journal of Sound and Vibration. 2004;**272**:1013–1032.

[14] Caracciolo R., Gasparetto A., Giovagnoni M. Measurement of the isotropic dynamic young's modulus in a seismically excited cantilever beam using a laser sensor. Journal of Sound and Vibration. 2000;**231**(5):1339–1353.

[15] Cortés F., Elejabarrieta M.J. Viscoelastic materials characterisation using the seismic response. Materials and Design. 2007;**28**:2054–2062.

[16] Liao Y., Wells V. Estimation of complex modulus using wave coefficients. Journal of Sound and Vibration. 2006;**295**:165–190.

[17] Beda T. Identification of viscoelastic fractional complex modulus. AIAA Journal. 2007;**42**(7):1450–1456.

[18] Kulik V.M., Semenov B.N., Boiko A.V., Seoudi B.M., Chun H.H., Lee I. Measurement of dynamic properties of viscoelastic materials. Experimental Mechanics. 2009;**49**:417–425.

[19] Maheri M.R., Adams R.D. Determination of dynamic shear modulus of structural adhesives in thick adherend shear test specimens. International Journal of Adhesion and Adhesives. 2002;**22**:119–127.

[20] Jahani K., Nobari A. Identification of dynamic (Young's and Shear) moduli of a structural adhesive using modal based direct model updating method. Experimental Mechanics. 2008;**48**:599–611.

[21] Hunston D.B. Viscoelastic characterization of structural adhesive via force oscillation experiments. Adhesion and Adsorption of Polymers. 1980;**12**:321–339.

[22] Deng S. Temperature-dependent elastic moduli of epoxies measured by DMA and their correlations to mechanical testing data. Polymer Testing. 2007;**26**:803–813.

[23] Ward I.M., Sweeney J., editors. An introduction to the mechanical properties of polymers. West Sussex: John Wiley and Sons; 2004.

[24] Ferry J.D., editor. Viscoelastic properties of polymers. 3rd ed. New York: John Wiley and Sons; 1980.

[25] Williams M., Landel R., Ferry J.D. The temperature dependence of relaxation mechanisms in amorphous polymers and other glass-forming liquids. Journal of the American Chemical Society. American Chemical Society. 1955;**77**:3701–3707.

[26] Segal E., Rosel J.L., editors. Nondestructive testing of adhesive bond joints. In: Sharpe RS, Research Techniques in Non-Destructive Testing, vol. IV. London: Academic Press; 1980.

[27] Fassbender R.H., Hagemaier D.J., Radeky R.L. Verification of defects found by nondestructive inspection in metallic adhesive bonded structures. International Journal of Adhesion and Adhesives. 1980;**1**(2):79–88.

[28] Biggiero G., Canella G. Ultrasonic testing for bond efficiency of carbon steel to stainless steel adhesive joints. International Journal of Adhesion and Adhesives. 1985;**5**(3):143–148.

[29] Assender H.E., Bowditch M.R., Gery N.F.C., Harris A.E., O'Gara P.M., Shaw S.J. A novel system for self-validating adhesive joints. International Journal of Adhesion and Adhesives. 2000;**20**:477–488.

[30] Chang D.J., Muki R. Stress distribution in a lap joint under tension-shear. International Journal of Solids and Structures. 1974;**10**:503–517.

[31] Michaloudaki M., Lehmann E., Kosteas D. Neutron imaging as a tool for the non-destructive evaluation of adhesive joints in aluminium. International Journal of Adhesion and Adhesives. 2005;**25**:257–267.

[32] Maev R.Gr., Titov S. Pulse-echo ultrasonic NDE of adhesive bonds in automotive assembly. In: ECNDT; Paris. France 2006.

[33] Chapman G.B., Sadler J., Maev R.Gr., Titov S., Maeva E.Y., Severina I., Severin F. Ultrasonic pulse-echo NDE of adhesive bonds in sheet-metal assemblies. In: IEEE Ultrasonics Symposium; Vancouver, Canada 2006. pp. 902–905.

[34] Da Silva L., Adams R., Gibbs M. Manufacture of adhesive joints and bulk specimens with high-temperature adhesives. International Journal of Adhesion and Adhesives. 2004;**24**:69–83.

[35] Wunderlich B., editor. Thermal analysis of polymeric materials. Berlin: Springer Verlag; 2005.

[36] Jones D., editor. Handbook of viscoelastic vibration damping. Wiley; New York, EEUU 2001.

[37] Rao M.D. Recent applications of viscoelastic damping for noise control in automobiles and commercial airplanes. Journal of Sound and Vibration. 2003;**262**:457–474.

[38] Banea M., Da Silva L. Mechanical characterization of flexible adhesives. The Journal of Adhesion. 2009;**85**:261–285.

[39] Kadioglu F., Adams R. Non-linear analysis of a ductile adhesive in the single lap joint under tensile loading. Journal of Reinforced Plastics and Composites. 2009;**28**:2931–2936.

[40] Chen T. Determining a Prony series for a viscoelastic material from time varying strain data. NASA Center for AeroSpace Information. Maryland, EEUU 2000.

[41] Bagley R.A. Theoretical basis for the application of fractional calculus to viscoelasticity. Journal of Rheology. 1983;**27**(3):201–210.

[42] Pritz T. Analysis of four-parameter fractional derivative model of real solid materials. Journal of Sound and Vibration. 1996;**195**(1):103–115.

[43] Oldham K.B., Spanier J., editors. The fractional calculus. New York: Academic Press; 1974.

[44] Lewandowski R., Chorazyczewski B. Identification of the parameters of the Kelvin-Voigt and the Maxwell fractional models, used to modelling of viscoelastic dampers. Computers & Structures. 2010;**88**:1–17.

[45] Haneczok G., Weller M. A fractional model of viscoelastic relaxation. Materials Science and Engineering. 2004;**370**:209–212.

[46] Alcoutlabi M., Martinez-Vega J. A modified fractional model to describe the viscoelastic behavior of solid amorphous polymers. The effect of physical aging Journal of Macromolecular Science, Part B. 1999;**38**:991–1007.

[47] Jia J., Shen X., Hua H. Viscoelastic behavior analysis and application of the fractional derivative Maxwell model. Journal of Vibration and Control. 2007;**13**:385–395.

[48] BoltzmannL. On the theory of the elastic aftereffect. Poggendorff's Annals of Physics and Chemistry. 1876;**7**:624–645.

[49] Nashif A.D., Jones D.I.G., Henderson J.P., editors. Vibration damping. New-York: Wiley Interscience; 1985.

[50] Roland C.M. Characteristic relaxation times and their invariance to thermodynamic conditions. Soft Matter. 2008;**4**:2316–2322.

[51] Emri I., Von Bernstorff B.S. Re-examination of the approximate methods for interconversion between frequency and time-dependent material functions. Journal of Non-Newtonian Fluid Mech. 2005;**129**:75–84.

[52] Park S.W., Schapery R.A. Methods of interconversion between linear viscoelastic material functions. Part I–A numerical method based on Prony series. International Journal of Solids and Structures. 1999;**36**:1653–1675.

[53] Park S.W., Schapery R.A. Methods of interconversion between linear viscoelastic material functions. Part II–An approximate analytical method. International Journal of Solids and Structures. 1999;**36**:1677–1699.

[54] Van Krevelen D.W., Te Nijenhuis K. Their numerical estimation and prediction from additive group contributions. In: Properties of Polymers: Their Correlation with Chemical Structure; Amsterdam, Netherlands 2009.

[55] Hatfield W.J., Quake Stephen R. Dynamic properties of an extended polymer in solution. Physical Review Letters. 1999;**82(**17) 3548–3560.

[56] Doi M., Edwards S.F., editors. The theory of polymer dynamics. Oxford: Clarendon; 1986.

[57] Mark E.J., editor. Physical properties of polymers handbook. New York, EEUU 2007.

[58] Ninomiya K., Ferry J.D. Some approximate equations useful in the phenomenological treatment of linear viscoelastic data. Journal of Colloid Science. 1959;**14**:36–48.

[59] Fernández P., Rodriguez D., Lamela M.J., Fernández-Canteli A. Study of the interconversion between viscoelastic behavior functions of PMMA. Mechanics of Time-Dependent Materials. 2010;**15**(2) 1–12.

[60] Schwarzl F. On the interconversion between viscoelastic material functions. Pure and Applied Chemistry. 1970;**23**:219–234.

[61] Sorvari J., Malinen M. Numerical interconversion between linear viscoelastic material functions with regularization. International Journal of Solids and Structures. 2007;**44**:1291–1303.

[62] Leblanc J. Transform rheometry: a new tool to investigate intrinsically non-linear viscoelastic materials. Annual Transactions of the Nordic Rheology Society. 2005;**13**:3–21.

[63] Bellanger M., editor. Digital processing of signals: theory and practice. New York: Wiley-Interscience; 1984.

[64] Cooley J., Tukey J. An algorithm for the machine calculation of complex Fourier series. Mathematics of computation. American Mathematical Society. 1965;**19**:297–301.

[65] Oran B., editor. The fast Fourier transform and its applications. Pretince Hall International; New Jersey, EEUU 1988.

[66] Dutt A., Rokhlin V. Fast Fourier transforms for nonequispaced data, II. Applied and Computational Harmonic Analysis. 1995;**2**:85–100.

[67] Fourmont K. Non-equispaced fast Fouriertransforms with applications to tomography. The Journal of Fourier Analysis and Applications. 2003;**9**:431–450.

[68] Greengard L., Lee J.Y. Accelerating the nonuniform fast Fourier transform. Siam review. Society for Industrial and Applied Mathematics. 2004;**46**(3):443–454.

[69] Marion D. Fast acquisition of NMR spectra using Fourier transform of non-equispaced data. Journal of Biomolecular NMR. 2005;**32**:141–150.

[70] Lee J.Y., Greengard L. The type 3 nonuniform FFt and its applications. Journal of Computational Physics. 2005;**206**:1–5.

[71] Adhikari S. Damping Models for Structural Vibration [thesis]. Cambridge University, Engineering Department: 2000.

[72] Adhikari S. Classical normal modes in non-viscously damped linear systems. AIAA Journal. 2001;**39**(5):1–3.

[73] García-Barruetabeña J., Cortés F., Abete J.M., Fernández P., Lamela M.J., Fernández-Cantelli A. Experimental characterization and modelization of the relaxation and complex moduli of a flexible adhesive. Materials and Design. 2011;**32**:2783–2796.

[74] Bies D., Hansen C., editors. Engineering noise control: theory and practice. London: Spon Pr; 2003.

[75] García-Barruetabeña J., Cortés F., Abete J.M., Fernández P., Lamela M.J., Fernadez-Cantelli A. Relaxation modulus-complex modulus interconversion for linear viscoelastic materials. Mech. Time-Depend Materials. 2013;**17**:465–479.

IntechOpen